공학석사학위논문

The Experimental Investigation of the Puffed Flame Structure and Characteristics by Using Simultaneous Laser Diagnostics

레이저 동시 계측을 이용한 Puffed 화염의 구조와 특성에 관한 실험적 연구

2019 년 2 월

서울대학교 대학원

기계항공공학부

임 대 홍

Abstract

The Experimental Investigation of the Puffed Flame Structure and Characteristics by Using Simultaneous Laser Diagnostics

Daehong Lim
School of Mechanical and Aerospace Engineering
The Graduate School
Seoul National University

To predict combustion instability, the study of the flame surface is necessary because there is a relationship between the heat release rate and the flame surface. Combustion instability is occurred and amplified when the three components of the perturbation constitute a positive feedback. Thus each of three components should be considered carefully. In order to predict the combustion instability, in this paper, the unique flame structure, called as 'the puffed flame', was investigated. In the previous work, Kim et al. [1]

discovered the puffed flame structure at the specific forcing frequency and the velocity perturbation region. In this paper, therefore, we revealed the causes and the dynamic characteristics of the puffed flame. Thus, simultaneous OH-PLIF and PIV measurements were conducted.

In case of the flame, the burke-schumann flame, a special case of the non-premixed flame, was considered. The mixture of the methane and hydrogen was used as the fuel, and the air was used as the oxidizer. The acoustic forcing was applied for the several frequency region; from 100 Hz to 180 Hz with 20 Hz steps. Also incoming velocity perturbation amplitude was varied from 0.1 to 0.5 with 0.1 steps.

The velocity, strain rate, and the distribution of the OH radical were measured at the same time due to the simultaneous laser diagnostics. From these results, the response characteristics and the flow behavior were found at the exact same time. Flame structure was captured from the OH-PLIF measurement and the other quantitative results such as velocity vector and strain rate field were measured from the PIV.

In the same forcing frequency region, the flame puffed phenomenon was occurred over the specific velocity perturbation amplitude. If the forcing

frequency became higher, the more velocity perturbation amplitude was necessary for the flame puffed. With this results, we could realize that the flame acts as a low pass filter. Also, it was revealed that the flame puffed phenomenon was periodic process which was following the external acoustic excitation wave.

With the simultaneous PIV and OH-PLIF results, we could find out the relative high strain rate and the oxidizer entrainment played important roles for the puffed process. High strain rate make flame wrinkle and flame throat more thinner. As the process proceeded, more higher strain rate was applied to the flame surface as well. At the final stage of the flame puffed phenomenon, highly irregular flow was generated, so that the strain rate became much higher.

Meanwhile, oxidizer entrainment could be another reason for the puffed flame. During the process, surrounding air was continuously invaded into the middle of the flame. At last, flame was separated into two regions due to the entrainment of the surrounding air.

When the flame puffed phenomenon was occurred, the dynamic characteristics became different from the non-excitation flame case. The

flame length became more smaller and the flame surface area also decreased. However, flame length and the surface area perturbation were increased. In other words, when the flame puffed, we could say that the flame became more unstable.

Keywords: Jet-diffusion flame, Burke-Schumann flame, Combustion instability, Flame structure, Simultaneous laser diagnostics, OH-PLIF, PIV, Response characteristics, Strain rate, Surrounding air entrainment, Flame separation

Student Number: 2017-29498

Contents

List of Tables

List of Figures

Chapter 1. INTRODUCTION

1.1 Combustion instability

From the early stage of the liquid rocket development, a combustion instability had been considered as one of the most important area for the combustion field. To avoid the development of the combustion instability is important for the combustion chamber structure and the output of the system. However, the precise prediction for the combustion instability has not been available yet. From the numerous researchers, there have been large amount of research for the combustion instability. Three sorts of the perturbations have been known as the causes of the combustion instability ; the acoustic oscillation, the flow oscillation, and the heat release oscillation. The acoustic oscillation means that the perturbation of the pressure in the combustion chamber. Also, the flow oscillation means that the oscillation of the injected flow due to the incoming perturbation of the fuel and the oxidizer. At last, the heat release oscillation is the perturbation of the heat release rate of the flame due to the flame surface perturbation. When one of the perturbations above

occurs, other two perturbations would be generated. It has been known that, at that time, if one perturbation make any other perturbations increase (positive feedback loop), the combustion instability occurs. When the combustion instability occurs with above interaction, the structure in the combustion chamber would be damaged due to the rapid growth of the heat release perturbation or pressure perturbation. Therefore, to investigate the combustion instability was necessary for the improvement of the performance and the stability for the system.

For the research area of the combustion instability, it could be divided in two sections. The first area is the prediction from the measurement and the second is the control. In this time, the prediction can also be divided into the analysis of the relationship, which is created between flow perturbation and heat release perturbation, and the analysis of the effect of the combustion chamber. In this time, heat release perturbation has a strong relationship with a flame surface perturbation. Thus, to investigate the change of flame structure due to the incoming velocity perturbation is one effort for the research of the relation between heat release rate perturbation and flow perturbation. In this research, we generated the arbitrary combustion

instability environment by applying the external acoustic excitation. Then we confirmed the response characteristics of the flame surface caused by the incoming velocity perturbation with the specific frequencies.

1.2 Strain rate

From the numerous research, it is well-known that the flame surface is strongly affected by the strain rate of the flame surface. When the strain rate is applied to the flame surface, flame surface is wrinkled then the flame surface area becomes larger. Because of the increase of the flame surface area, the chemical reaction rate of the flame also increases. In this process, the strain rate which is applied during such residence time makes the flame surface thinner and highly wrinkled. Donbar et al. [11] confirmed that the ratio of the flame surface could be expressed as Eq. (1).

$$A_2/A_1 = exp(K_s \cdot t_{res}) \qquad (1)$$

In Eq. (1), A_1 and A_2 was defined as the flame surface area before and after the strain rate was exerted. Each of the relative time rate of change in flame front and the residence time was marked as K_s and t_{res}. Especially, Carrier et al. [28] verified analytically that the flame surface of the non-premixed flame was determined by the strain rate. Several studies [12-17] discovered the relationship between strain rate and the flame surface as well.

Strain rate effect can be divided into two regions. The first is the effect of

the oscillatory strain rate and the second is the effect of the steady strain rate. When the strain rate oscillates on the flame surface with the specific frequency, the response characteristics of the flame surface to the strain rate would be changed due to the oscillating frequency regions. The case with low frequency oscillation, first of all, the response characteristics is as same as that of the case with the steady strain is applied. For the case of the moderate oscillating strain rate, the flame surface responses with such time lag from the strain rate oscillation. In other words, there is such phase shift between the strain rate oscillation and the response of the flame surface. However, for the case of the strain rate oscillation with high frequency, the flame surface has unresponsive characteristics for the strain rate oscillation. Also, it is more effective for the flame quenching than the oscillatory strain rate, when the steady strain rate is applied to the flame surface.

When the flame surface is under the strained flow environment, the element motion of the line segment of the flame surface could be sorted into three motions; translation, rotation, and strain. In this time, the translation motion and the rotation motion are intimately related with mixture's motion, while to change the internal structure of the flame is due to the strain. This strain

motion could be expressed as Eq. (2).

$$\boldsymbol{\varepsilon} = \frac{\mathbf{1}}{|\boldsymbol{\delta\ell}|}\frac{\boldsymbol{d\delta\ell}}{\boldsymbol{dt}} = \frac{\boldsymbol{\delta\ell\cdot\nabla u}}{|\boldsymbol{\delta\ell}|} \qquad (2)$$

When two axes, x and y axes, are set on the flame surface, x-axis is parallel with the flame surface and the y-axis is perpendicular with the x-axis. Thus the line segment of the flame surface can be divided in two components, ℓ and m. The component ℓ is aligned with the x-axis, while the component m is coincident with the y-axis.

At the initial time, the line segment can be projected on the axes as Eq. (3) and (4).

$$\boldsymbol{\ell_x(t) = \ell(t), \ell_y(t) = 0} \qquad (3)$$

$$\boldsymbol{m_x(t) = 0, m_y(t) = m(t)} \qquad (4)$$

After the time dt is passed, the line segments can be expressed as,

$$\boldsymbol{\ell_x(t+dt) = (1 + \frac{\partial u}{\partial x}dt)\cdot \ell(t)} \qquad (5)$$

$$\boldsymbol{\ell_y(t+dt) = \left(\frac{\partial v}{\partial x}dt\right)\cdot \ell(t) = 0} \qquad (6)$$

$$\boldsymbol{m_x(t+dt) = \left(\frac{\partial u}{\partial y}dt\right)\cdot m(t)} \qquad (7)$$

$$\boldsymbol{m_y(t+dt) = \left(1 + \frac{\partial v}{\partial x}dt\right)\cdot m(t)} \qquad (8)$$

In this time, u and v are the velocity components for the of the flow for

the x and y axes. With these above equations, pure shear flow, which corresponds to a component of the strain rate, can be expressed as Eq. (9).

$$\boldsymbol{\tau_{xy}} = \frac{1}{2}\left(\frac{\partial u}{\partial y} + \frac{\partial v}{\partial x}\right) \qquad (9)$$

In this research, the strain rate was calculated with Eq. (9) and the vector field resulted from the Particle Image Velocimetry.

1.3 Previous research

Combustion instability and the flame structure have been frequently researched. Kim et al. [1] determined the effect of the external acoustic forcing for the burke-schumann flame. Also, they discovered the puffed flame phenomenon for the burke-schumann flame in the specific forcing frequency region. Hwang et al. [2] conducted the experiments for identifying the flame stabilization and the relation between the flame length and the emission. Ahn et al. [3] figured out the flame response characteristics by determining the flame describing function.

For the flame structure analysis, the laser diagnostics has been used to investigate the molecular location and confirm the properties of the combustion field. Rossel et al. [4] performed simultaneous several molecule PLIF method for detect each of the flame region. Shimura et al. [5] conducted simultaneous dual plane CH-PLIF, single plane OH-PLIF, and dual plane stereoscopic PIV measurements to investigate three-dimensional flame structure. Tanahashi et al. [6] applied the simultaneous CH-OH PLIF and stereoscopic PIV to confirm the local flame structure of turbulent premixed

flame. Elbaz et al. [7] determine the flame characteristics and structure of the inverse diffusion flame by using 10kHz OH and acetone PLIF. Lakshminarasimhan et al. [8] compared the flame structure for the acoustic forcing in case of the resonance forcing, second harmonic forcing, off-resonance forcing, and without forcing. Rehm et al. [9] also used the simultaneous PIV and OH-PLIF measurement to analyze the combustion field. They described the relationship between the flame surface, the strain rate, and the vorticity. They confirmed that the vorticity was well correlated with the flame surface. Salaün et al. [10] conducted simultaneous PIV and OH-PLIF measurement in model gas turbine combustor. They analyzed the flame splitting temporally and confirmed the flame splitting mechanism, then considered the strain rate as the important factor for the flame splitting phenomenon. Donbar et al. [11] announced that the oscillated strain rate with the low frequency only affected the flame surface by the results of the simultaneous PIV and CH-PLIF. They explained that the flame separation phenomenon with the vortical flow and the oxidizer entrainment. Besides these above researches, many of other researchers [12-17] have been studied about the strain rate and the flame splitting phenomenon.

Also, buoyancy effect acts as a key for determining the flame structure. It should be considered during the analysis about the non-premixed flame structure. There were several studies [18-22] about the buoyancy effect for the non-premixed flame. Mostly, the buoyancy induced instability caused the vortex generation and the flame stretch.

Especially, Hou et al. [23] numerically and experimentally confirmed the response characteristics of the jet diffusion flame. With the high speed images, they verified the progress of the puffed flame process. Yoshihara et al. [24] found out the response characteristics of the pool fire at the low gravity environment. Abe et al. [25] studied for the puffing phenomenon of the liquid pool fire. Liao et al. [26] confirmed the flame puffed phenomenon under the strongly pulsed acoustic forcing for the swirled jet diffusion flame. Carpio et al. [27] analyzed the effect of the several non-dimensional number for the flame pinch-off numerically.

According to previous works, we employed the simultaneous PIV and OH-PLIF laser diagnostics for determining the flame characteristics and structure. In addition, with the simultaneous results, we focused on the strain rate effect and the oxidizer movement to reveal the causes of the flame puffed

phenomenon.

Chapter 2. EXPERIMENTAL APPARATUS AND METHODS

2.1 Burke-schumann flame combustor

The response characteristics and the flame surface perturbation of the burke-schumann flame against the acoustic forcing were analyzed in this research. Burke-schumann flame is one of the special cases for the laminar, coaxial non premixed flame, and it has the same exit velocity for the fuel and the oxidizer nozzles. In the previous paper, Kim et al. [1] found out the flame puffed phenomenon but did not confirm for the causes of the puffed flame.

Figure 2.1 is the burke-schumann flame combustor which could found out the response characteristics for the external acoustic excitation. To supply the fuel and the oxidizer, the fuel feed line and the oxidizer feed line is connected to the combustor. The fuel and oxidizer nozzles which are directly attached to the combustion chamber have the circular cross section. Two nozzles are arranged coaxially with the diameter of 5mm for the fuel nozzle and 50mm for the oxidizer nozzle. The combustion chamber, which is made with

rectangular quartz, is mounted on the tip of the fuel and oxidizer nozzle.

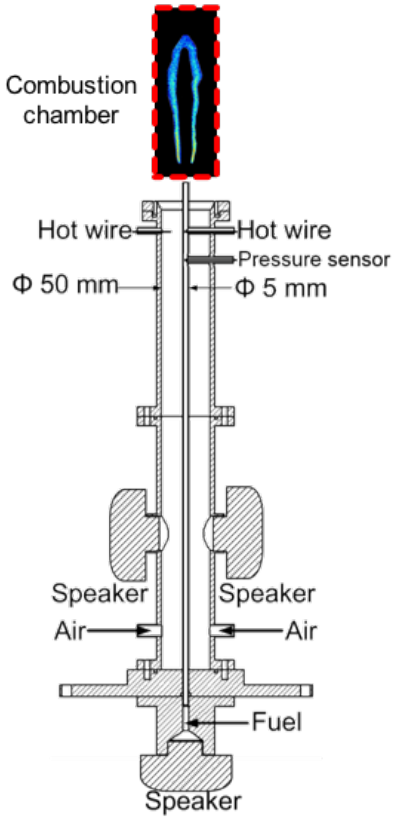

Figure 2.1 Schematic of a cross-section of
a Burke-schumann flame combustor.

2.2 Test condition

In this research, the mixture of the hydrogen and the methane was used as fuel for the burke-schumann flame. The fuel was composed of 75% of hydrogen and 25% of methane. The dried air with room temperature was used as the oxidizer. Also, the exit velocity of the fuel and air were fixed in 1m/s to produce the burke-schumann flame. The mass flow rate of the hydrogen was 0.89 slpm and that of the methane was 0.3 slpm, while that of the air was 214 slpm. The mass flow rates of the fuel and air were controlled by the Mass Flow Controller (MFC). Acoustic forcing for the both fuel and air were conducted by the three loudspeakers. Two loudspeakers were equipped both sides of the oxidizer feed pipe to acoustically excite the incoming air and the other one loudspeaker was mounted under the fuel feed line to excite the incoming fuel. These speakers were operated and controlled by the function generator to make appropriate velocity perturbation amplitude and the wave form. In this time, hot wire anemometry (HWA) was adopted to identify the fuel and air velocity distribution and the phase of the acoustic forcing. When the acoustic forcing was employed, forcing frequency was varied from 100 Hz

to 180 Hz with 20 Hz steps. Meanwhile, the acoustic forcing amplitude, which was indicated by the velocity perturbation per mean velocity, was varied from 0.10 to 0.50 with 0.1 steps. The velocity perturbation amplitude is calculated as Eq. (10).

$$velocity\ perturbation\ amplitude = {u'}/{\bar{u}} \qquad (10)$$

The test condition of this research was minutely shown in Table 2.1.

Table 2.1 Experimental condition.

Parameter	**Value**
Fuel and Oxidizer	H_2 / CH_4, air
Composition of the fuel	$H_2 : CH_4 = 75 : 25$
Velocity of the air	$1m/s$
Velocity of the fuel	$1m/s$
Supply rate of the air	$214\ slpm$
Supply rate of the fuel	$H_2 : 0.89\ slpm\ (75\%)$
	$CH_4 : 0.3\ slpm\ (25\%)$
Acoustic forcing frequency [Hz]	$100, 120, 140, 160, 180$
Velocity perturbation amplitude	$0.1, 0.2, 0.3, 0.4, 0.5$

slpm : standard liter per minuite (L/min)

In addition, Froude number, which is one of the non-dimensional number, plays a key role in the non-premixed flame. Froude number is determined as Eq. (11).

$$Fr = {U^2}/{(g \cdot Rf)} \qquad (11)$$

Froude number is the representative non-dimensional number of the buoyancy effect for the non-premixed flame. However, in the present study, we did not largely concerned about the buoyancy effect. When the Froude number is larger than 1, the flame is known as the momentum dominant. Whereas, if the Froude number is smaller than 1, the flame behaves as buoyancy dominant. When the Froude number comes to zero, the buoyancy induced unstable phenomenon in the flame disappears. In this research, Froude number for the puffed flame case is about 32.4, so we decided that the puffed flame had the momentum dominant behavior. Thus, we neglected the buoyancy effect for the analysis of the puffed flame in this research.

Meanwhile, the other important non-dimensional number is the Lewis number. In this research, we were focused in the reason of the puffed flame which was related to the flow characteristics. We assumed, therefore, that the

Lewis number equals one.

2.3 Particle image velocimetry

Particle image velocimetry (PIV) is the laser diagnostics which can determine the velocity field and other properties of the combustion field with the particle injection. For the PIV measurement, the assumption that the particle totally follows the flow is necessary. For this assumption, the particle which has small enough diameter should be injected to the combustion field. Also, particle should be injected with such quantity that does not change the characteristics of the flow field. After the particle injection, the two pulses of the laser sheet is shot into the combustion chamber with the time interval, Δt. Then two of the mie scattering images of the seeding particle in the combustion field can be acquired. With the post processing between these two images, the velocity vector field can be obtained with calculating the distance from each seeding particle's movement during the time interval, Δt. In this research, two dimensional PIV measurement was conducted with the laser sheet. Thus, we could not acquire the orthogonal component of the laser sheet and it is the limitation of this research.

We used the ZrO_2, which had a diameter of $1\mu m$, as a seeding particle and

the interrogation cell size was 32 pixel by 32 pixel. It was known that the each of the particle's distance between laser beam A and B should be smaller than the quarter of the interrogation cell size. Thus, we set the interval between the beam A and B as $300\ \mu s$. Detailed condition of the PIV is shown in Table 2.2.

Table 2.2 Detailed experimental condition of the PIV.

Parameter	**Value**
Sampling rate	$1000\ Hz$
Particle	ZrO_2
Diameter of the particle	$1\ \mu m$
Interrogation cell size	$32\ pixel\ by\ 32\ pixel$
Velocity range	$0.5 \sim 1.5\ m/s$
Real length per pixel	$0.06\ mm$
Quarter of the interrogation cell size	$0.481\ mm$
Delay between beam A and B	$300\ \mu s$
$1.5\ m/s\ (\text{max.}\ velocity) \times 300\ \mu s$	$0.45\ mm$

Double pulsed ND:YLF laser (Photonics, DM20-527DH, $527nm$, $22.5mJ$, $10kHz$) was used as the PIV laser. 1000 image sets were obtained during 1 second with the high speed CMOS sensor (Photron, SA5 High speed CMOS). In Fig. 2.2, the raw image and the post-processed image for the PIV measurement were shown.

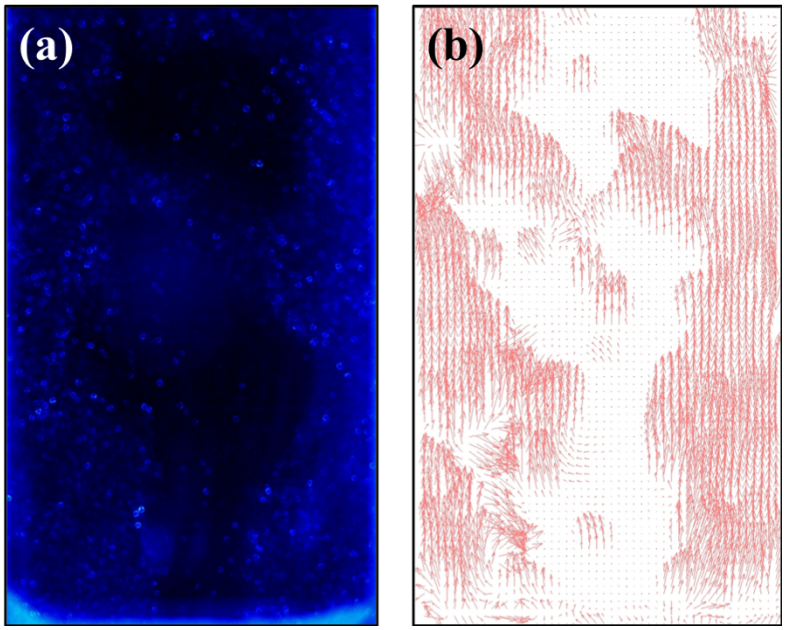

Figure 2.2 The example images for the PIV measurement.
(a) raw image (b) calculated vector field.

2.4 OH-Planar laser induced fluorescence

OH-Planar laser induced fluorescence (OH-PLIF) is the laser diagnostics which can determine the reaction zone effectively. Following is the process of the OH-PLIF measurement. First of all, injected laser beam forcibly excites the OH radical which is produced during the combustion process. Then we can measure the concentration of the OH radical by detecting the emitted light when the relaxation is occurred. In this time, injected laser beam should have the wavelength of $283\,nm$ and the emission light has a wavelength of around $310\,nm$. OH radical has huge amount of concentration at the burned gas region, so we can determine the flame structure. However, the fact that the CH radical acts as better zone marker than the OH radical is well-known. CH radical is performed in two body reaction, whereas the OH radical in third body reaction. This makes the CH radical removes more faster. Thus, the detected flame surface with CH-PLIF is around three times thinner than that of the case of OH-PLIF. With the earlier research, however, we could found out that the flame surface from CH-PLIF was located in the innermost region of the flame surface from OH-PLIF. Eventually, the flame surface from OH-

PLIF includes the flame surface from CH-PLIF. Because the major purpose of this research is to analyze the movement of burke-schumann flame due to the acoustic forcing, we employed the OH-PLIF measurement.

OH-PLIF system is composed of the ND:YAG laser (Edgewave, IS 200-2L, $1024\ nm$) as a pump laser, the tunable dye laser (Sirah, Credo, $275 \sim 370\ nm$), the high speed CMOS sensor (Photron, SA5 High speed CMOS), and the intensifier (Lavision, High speed IRO). Although $7.5\ kHz$ image acquisition with maximum spatial resolution ($1024 * 1024$) was possible, 1 kHz measurement was conducted in this research. Figure 2.3 shows OH distribution (i.e. reaction zone) by using OH-PLIF measurement.

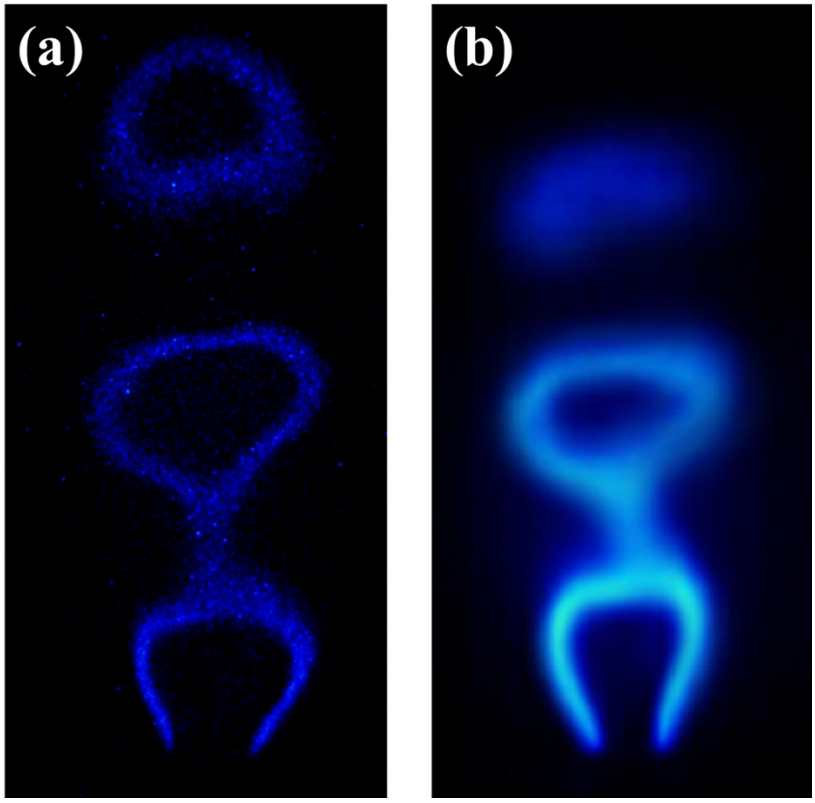

Figure 2.3 The result images for the OH-PLIF.
(a) instantaneous image (b) averaged image (1sec).

2.5 Simultaneous laser diagnostics

Periodic (appeared with the wave form of external acoustic forcing) flame puffed phenomenon was studied in this research. To understand the periodic phenomenon and its reason, time resolved simultaneous results are necessary. Thus we applied the simultaneous laser diagnostics of OH-PLIF and PIV to analyze the flame structure, surrounding flow movement, and the other properties. By employing simultaneous measurement, we could found out both the flame structure and the characteristics at the exact same time. For the simultaneous measurement, the timing of the laser sheet injected to the combustion chamber should be considered. Thus, the timing diagram of the laser beams is expressed in Fig. 2.4. Because of the execution of the simultaneous measurement, the laser beam for the OH-PLIF was located between the laser beam A and B for the PIV measurement. In Fig 2.5, simultaneous OH-PLIF and PIV laser system is shown.

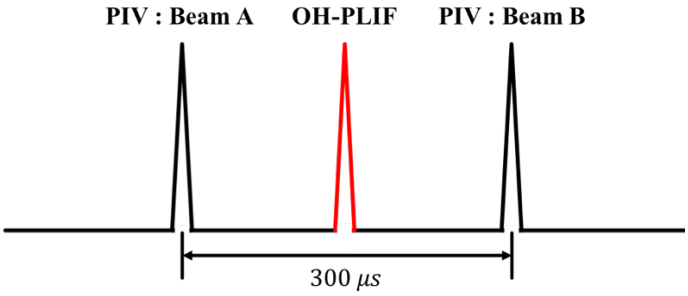

Figure 2.4 Timing diagram of the simultaneous measurement.

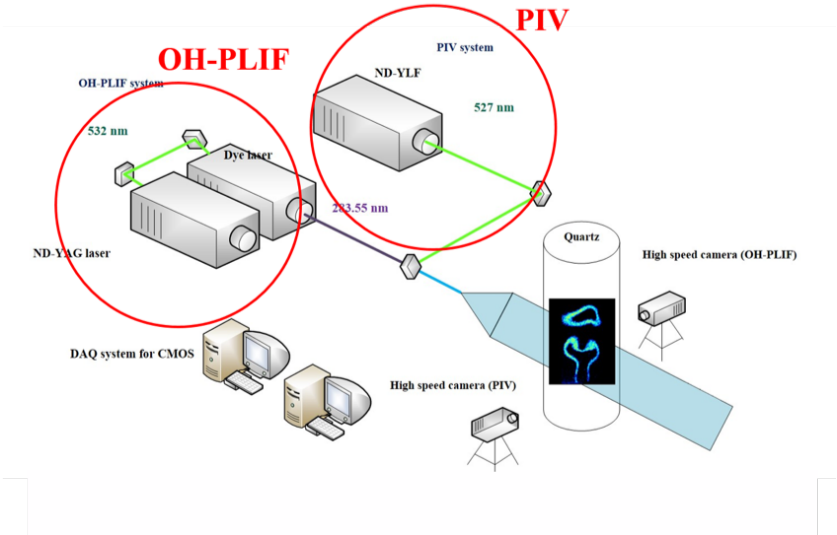

Figure 2.5 The laser system of the simultaneous measurement.

Chapter 3. Results and Discussion

3.1 OH-PLIF images for the puffed flame

3.1.1 OH-PLIF images for the various forcing frequencies

The flame structure was analyzed by using OH-PLIF measurement. In this chapter, the flame response characteristics was confirmed with varying the acoustic forcing frequency without changing the incoming velocity perturbation. While applying the external acoustic excitation, the incoming velocity perturbation amplitude was limited to 0.3 (amplitude was 30% of the average velocity), and the forcing frequency was increased from 100 Hz to 180 Hz with 20 Hz steps. In Fig. 3.1, the flame behavior is divided in six phases for the various forcing frequencies. The images were averaged from 100 images in the same phase of the acoustic forcing. The effect of the forcing frequency toward the flame could be analyzed by these images. Under the condition with the velocity perturbation amplitude of 0.3, the flame separated into two regions in the range of 100 Hz to 140 Hz of the forcing frequency.

For the separated flame, each of the lower and upper parts of the flame could be called as the major flame region and the secondary flame region. In the range of 160 Hz to 180 Hz, however, there were significant flame surface perturbation, but not enough perturbations for the flame puffed phenomena were detected. For these results, we could know that the flame puffed phenomenon was easily occurred at the lower forcing frequency region. We could also confirmed that the flame act like a low pass filter with this analysis.

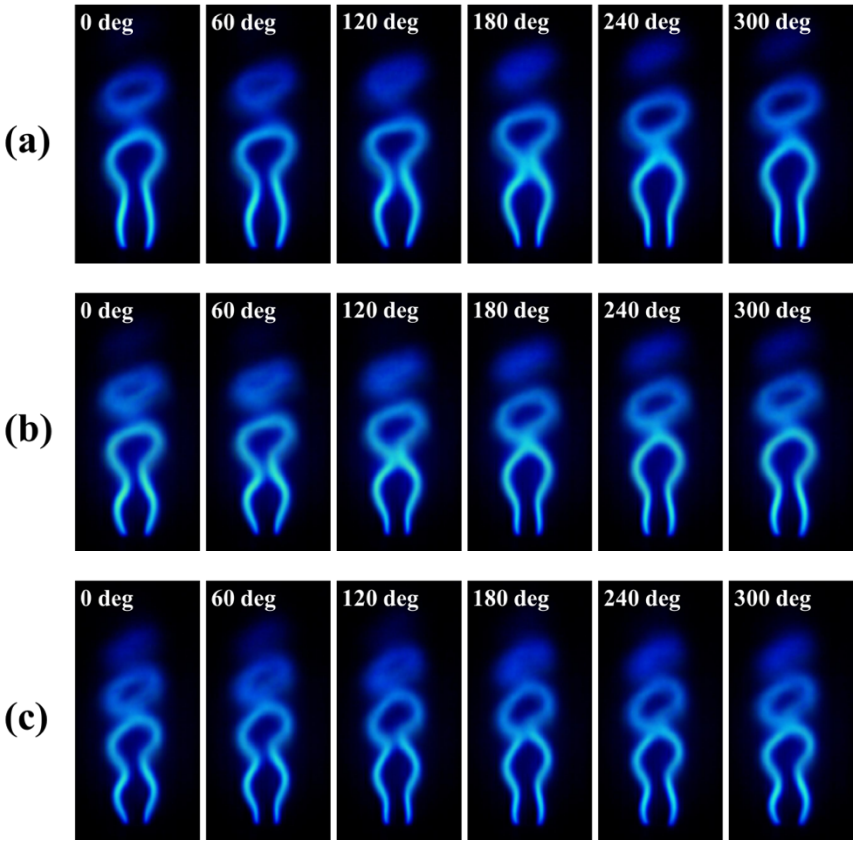
(a)
0 deg
60 deg
120 deg
180 deg
240 deg
300 deg
(b)
0 deg
60 deg
120 deg
180 deg
240 deg
300 deg
(c)
0 deg
60 deg
120 deg
180 deg
240 deg
300 deg

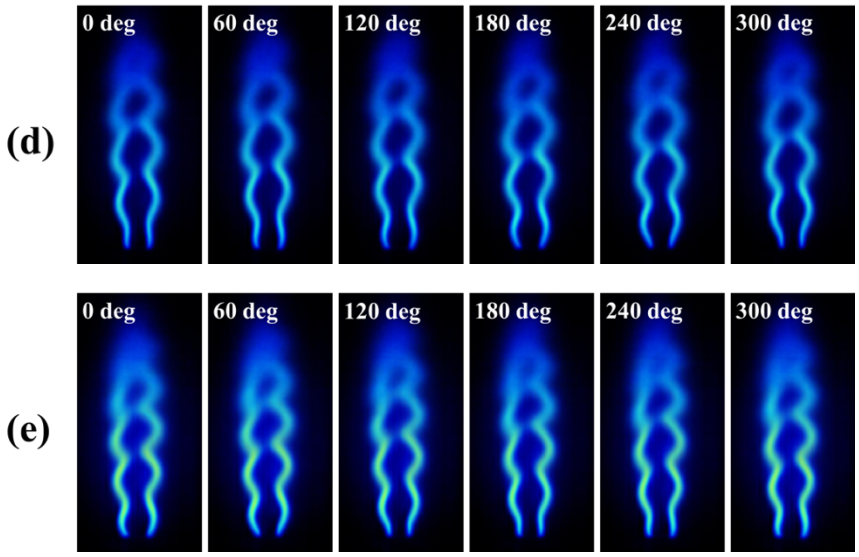

Figure 3.1 The averaged images for the various forcing frequencies with the velocity perturbation amplitude of 0.3. (a) 100 Hz (b) 120 Hz (c) 140 Hz (d) 160 Hz (e) 180 Hz

3.1.2 OH-PLIF images for the various velocity perturbation amplitudes

In this section, the result of the OH-PLIF images for the various velocity perturbation amplitude is shown. The effect of the incoming velocity perturbation amplitude was exhibited in Fig. 3.2. The images were also averaged from 100 images like previous paragraph. The forcing frequency was restricted as 100 Hz and only the incoming velocity perturbation amplitude was changed. For this experiment, we could verify the effect of the velocity perturbation amplitude. As the velocity perturbation amplitude increased, the flame surface perturbation also rose. Therefore, for the cases where the velocity perturbation were 0.3 and over, we could find out the flame puffed phenomena were occurred. Thus, the flame was separated into the major region and the secondary region due to the significant flame surface perturbation. Eventually, we determined that the incoming velocity perturbation amplitude was strongly affected to the flame puffed phenomenon.

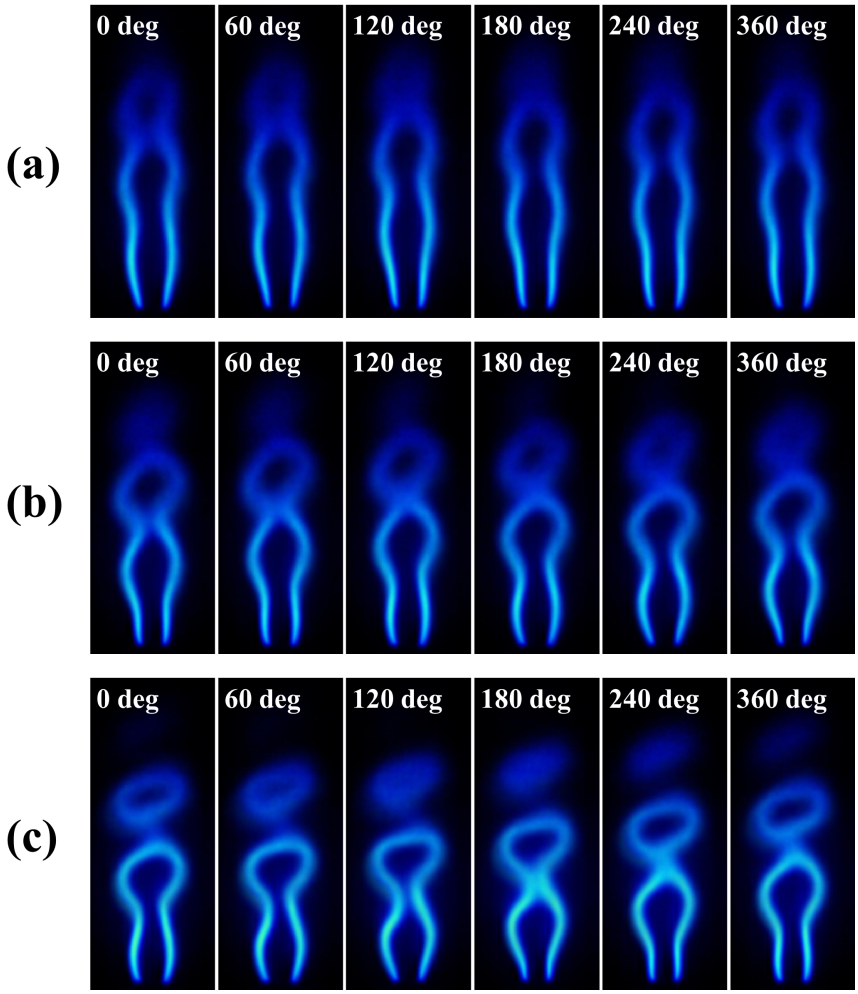
(a)
0 deg
60 deg
120 deg
180 deg
240 deg
360 deg
(b)
0 deg
60 deg
120 deg
180 deg
240 deg
360 deg
(c)
0 deg
60 deg
120 deg
180 deg
240 deg
360 deg

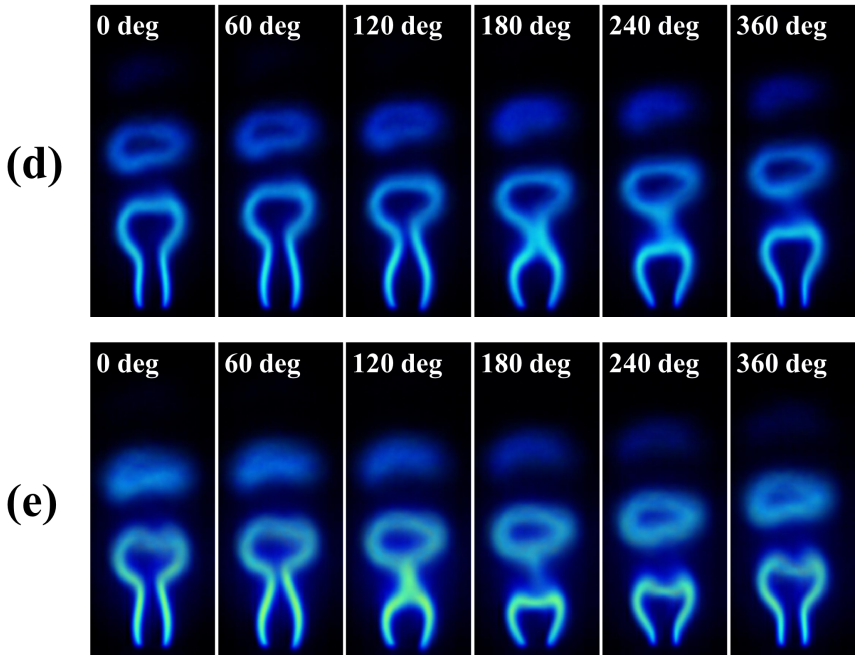

Figure 3.2 The averaged images for the various velocity perturbation amplitudes with the forcing frequency of 100 Hz.

(a) $u'/\bar{u} = 0.1$ (b) 0.2 (c) 0.3 (d) 0.4 (e) 0.5

3.1.3 Averaged OH-PLIF images

During the flame puffed phenomenon, the images with the same phase were averaged along the 100 cycles. There were specific repetitions with the phases of the external acoustic wave. The averaged images for 100 Hz of the forcing frequency and 0.4 of the velocity perturbation amplitude were shown in Fig. 3.3 (a) ~ (f). Applying the external acoustic forcing, the flame structures of Fig. 3.3 (a) ~ (f) were appeared periodically. At Fig. 3.3 (a), flame started to wrinkle. As the process proceeded, the flame surface perturbation was intensified. Finally, at Fig. 3.3 (f), flame was separated into two regions. Thus, we found out that the flame puffed phenomenon was following the acoustic forcing frequency.

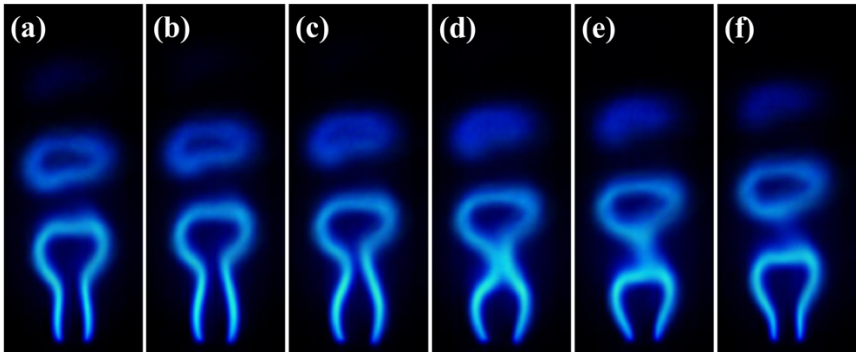

Figure 3.3 The averaged images for the puffed flame.
(a) 0 deg (b) 60 deg (c) 120 deg
(d) 180 deg (e) 240 deg (f) 300 deg

3.2 Results of the simultaneous laser diagnostics

3.2.1 Radial velocity generation

As the external acoustic forcing was applied to the flame, the flame behaved periodically. At the beginning of the flame puffed process, radial velocity component was generated near the nozzle exit. With the temporal analysis of the simultaneous laser diagnostics results, we found out that there existed periodic repetition of the suction phase and the release phase. The suction phase is shown in Fig. 3.4 (a), and the release phase is shown in Fig. 3.4 (b). When the suction phase was occurred, some portion of the surrounding air flowed into the fuel nozzle. Meanwhile, the radial velocity component of the surrounding air, which was on the way to the fuel side from the air side, was generated. Whereas, in the release phase, there were no surrounding air intrusion toward the fuel region, so the radial velocity components which were heading to the air side were dominant in the surrounding air flow.

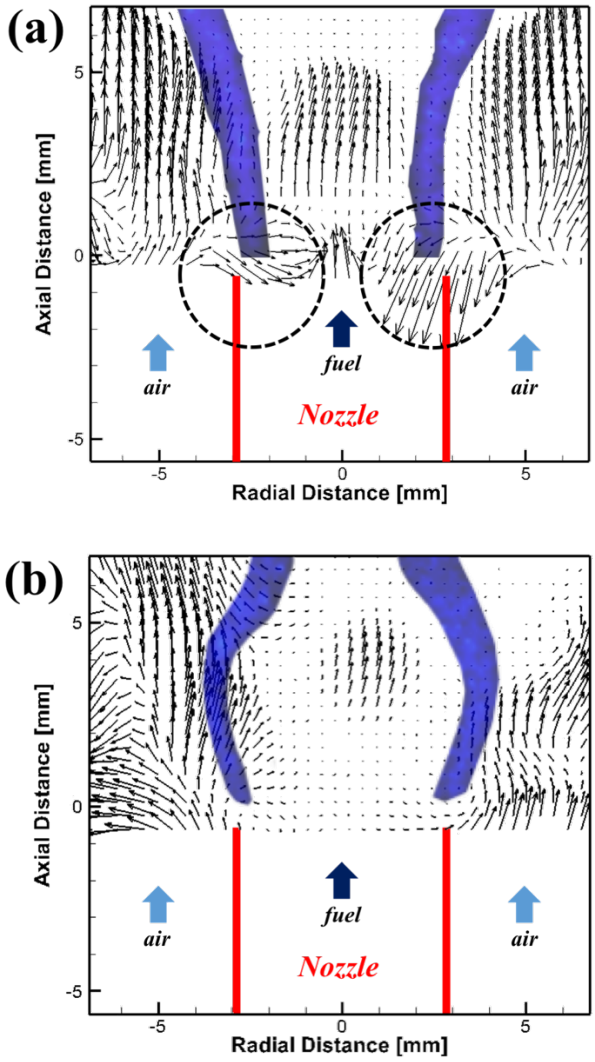

Figure 3.4 Simultaneous measurement results for (a) suction phase (b) release phase

The occurrence of the suction phase and the release phase was caused by the dynamic pressure and the velocity perturbation of the fuel nozzle. In Fig. 3.5, the pressure perturbation profile and the velocity profile at the fuel nozzle exit were plotted. At that time, the dynamic pressure perturbation was determined as Eq. (12).

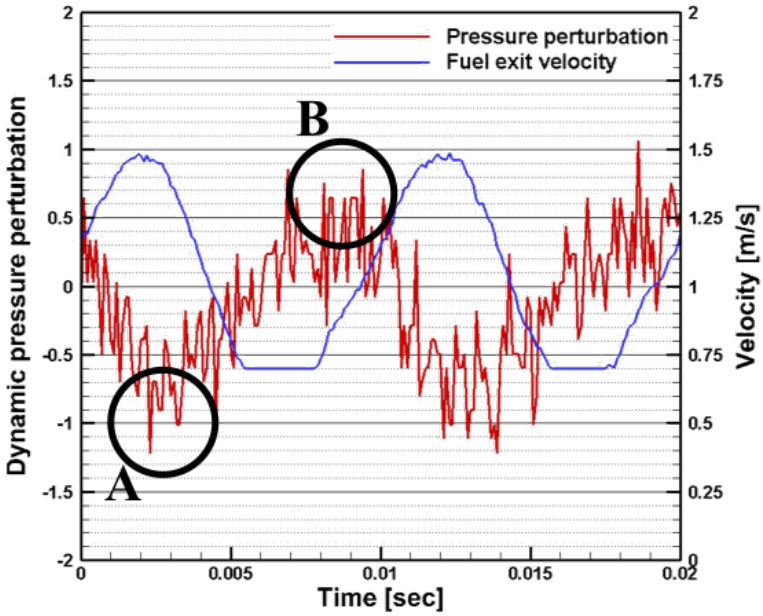

Figure 3.5 The pressure perturbation and the velocity profile at the nozzle tip.

$$Dynamic\ Pressure\ Perturbation \equiv {q'}/{|\bar{q}|} \qquad (12)$$

The phase difference of the dynamic pressure perturbation profile and the velocity profile was due to the difference between the measurement points. The suction phase was marked as A in the plot, and the release phase was marked as B. At that time, when the dynamic pressure perturbation had the lowest value, the suction phase was occurred and some portion of the surrounding air was entrained to the fuel nozzle. Also the mass flow rate of the fuel was the minimum. After half period of the wave, the release phase was occurred and there was no suction of the surrounding air. The repetition was lasted while the external acoustic forcing was applied. With repetition of these two phases, the dominant direction of the radial velocity of the flow was continuously changed. Thus, the downstream flow was significantly affected by this process.

3.2.2 The beginning of the flame surface wrinkling

The radial velocity generated by the repetition of the suction phase and the release phase strongly affected downstream. Flame was started to wrinkle because the surrounding air pushed the flame front toward the centerline of the fuel nozzle, as shown in Fig. 3.6 (a). The relative high strain rate due to the irregular flow movement could be detected as well in Fig. 3.6 (b).

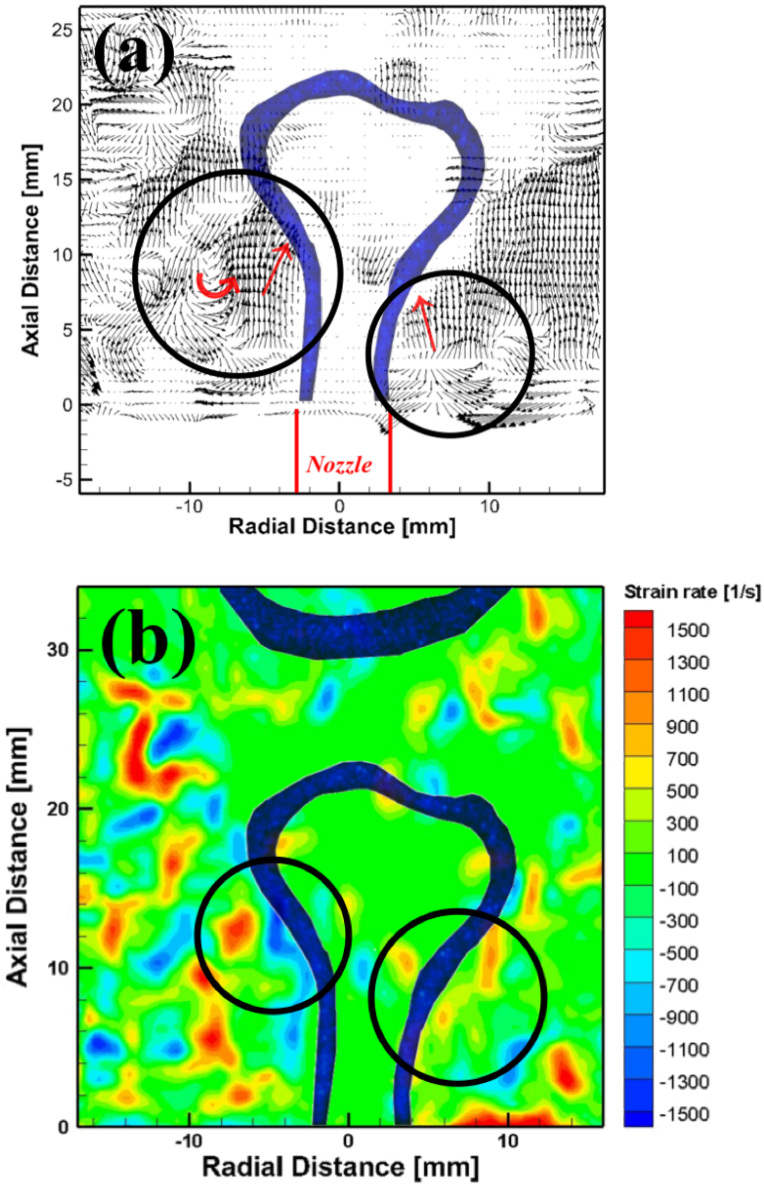

Figure 3.6 The velocity vector and the strain rate field when the flame started to wrinkle.

3.2.3 Strain rate distribution near the critical region

The whole range of the strain rate field and the reaction zone were temporally analyzed in Fig. 3.7 (a) ~ (h). First off all, the flame puffed process could be divided in 3 regions; undeveloped region, transient region, and fully puffed region. 1 cycle of the flame puffed phenomenon was taken place during 10ms, $t = 0ms$ to $t = 9ms$. The time duration of $t = 0ms$ to $3ms$ could be called as undeveloped case, the time duration of $t = 7ms$ to $9ms$ could be called as fully puffed case, and the case between them could be called as transient case. In this paper, however, we analyzed the time duration only in $t = 1ms$ to $8ms$, because this interval was a key range for the flame puffed phenomenon. Thus, the cases that $t = 1ms$ to $t = 3ms$ (i.e. Figure 3.7 (a) to (c)) could be expressed as the undeveloped case when the flame surface was only wrinkled, and $t = 7ms$ to $8ms$ cases (i.e. Figure 3.7 (g) to (h)) were the fully puffed case when the flame puffed phenomenon was perfectly occurred. With Fig. 3.7, we could analyzed that more higher strain rate was applied to the flame as the flame puffed process was proceeded, in the qualitative perspective. Being applied more higher strain rate on the flame

surface, the flame finally separated into the major region and the secondary region at $t = 7ms$, in Fig. 3.7 (g).

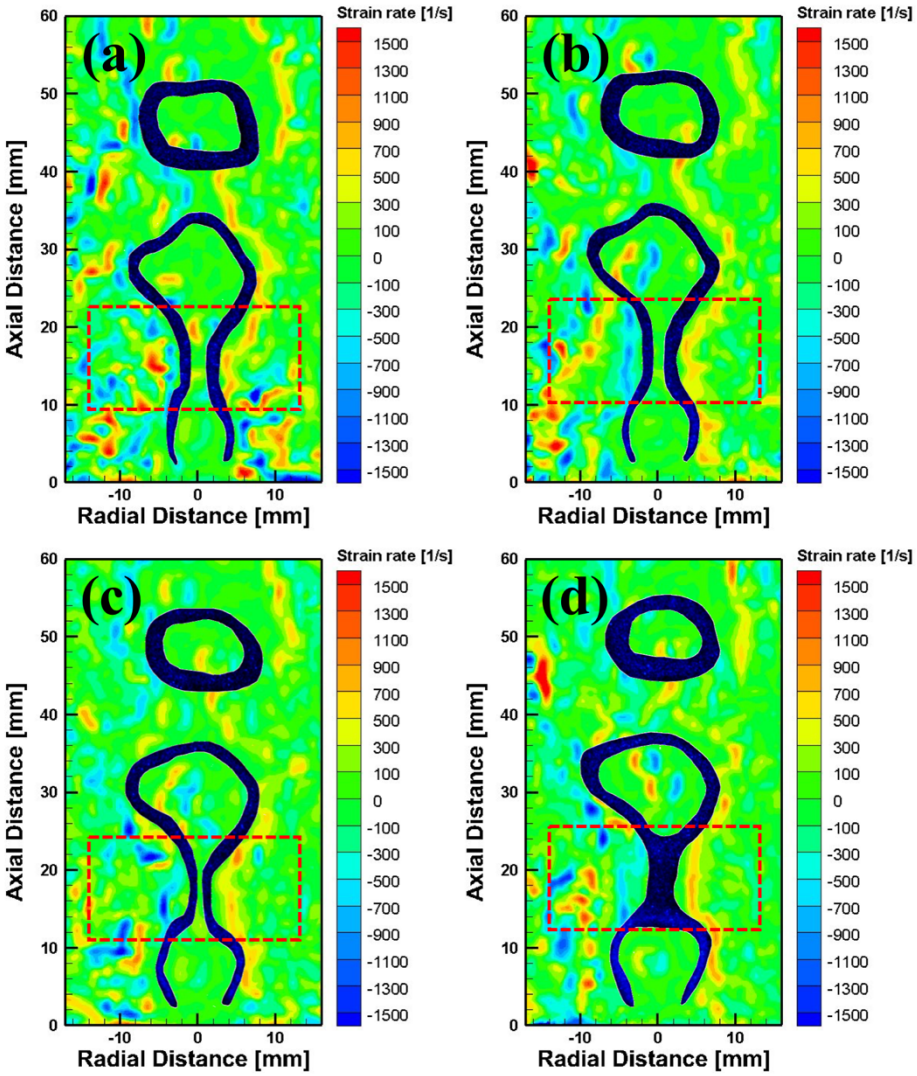
(a)
(b)
(c)
(d)
Strain rate [1/s]
1500
1300
1100
900
700
500
300
100
0
-100
-300
-500
-700
-900
-1100
-1300
-1500
Axial Distance [mm]
Radial Distance [mm]
0
10
20
30
40
50
60
-10
0
10

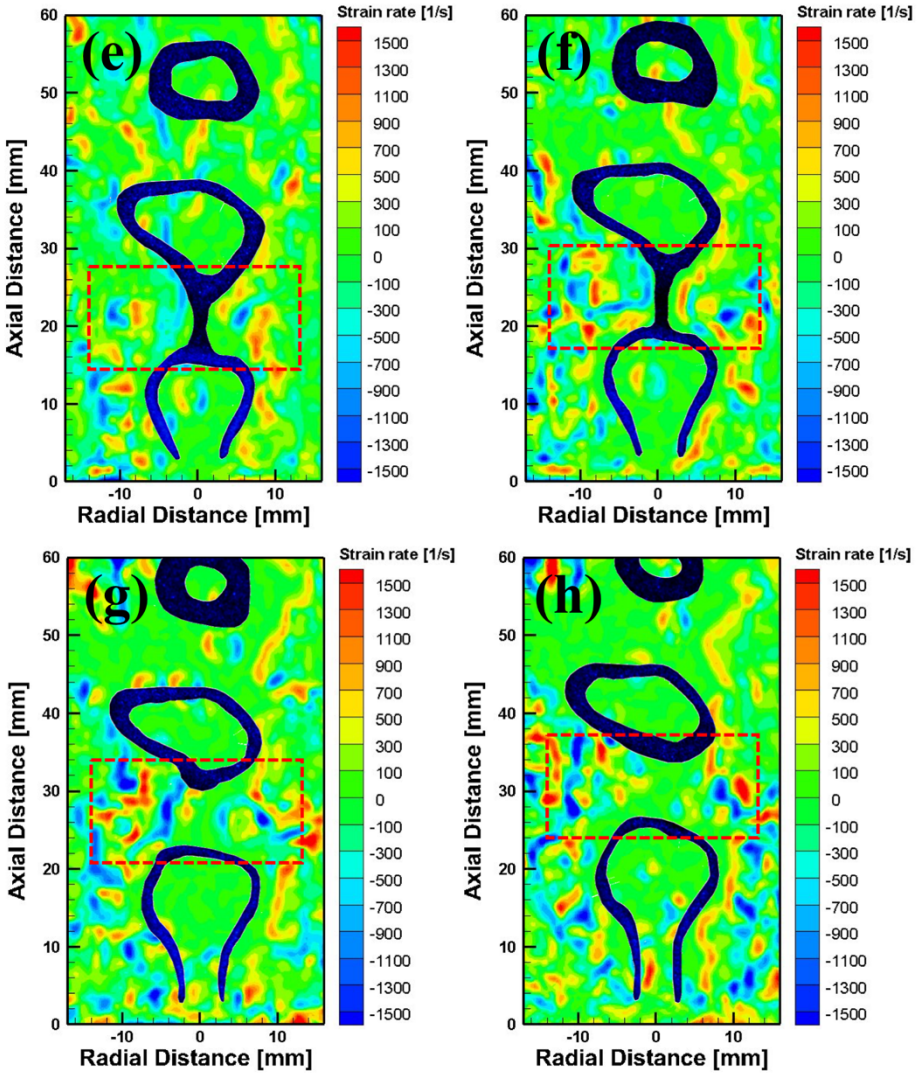

Figure 3.7 The temporal analysis of the flame puffed phenomenon with the strain rate and the flame surface.
(a) $t = 1ms$ (b) $2ms$ (c) $3ms$ (d) $4ms$
(e) $5ms$ (f) $6ms$ (g) $7ms$ (h) $8ms$.

In Fig. 3.8 (a) ~ (h), the critical regions of the flame puffed phenomenon were shown. We could know that more higher strain rate was applied near the flame throat (the area which was about to cut during the flame puffed phenomenon). Then the strain rate could be one of the reasons of the flame puffed phenomenon. As the process proceeded, high strain rate continuously invaded the flame throat area, and the flame throat thickness was gradually decreased.

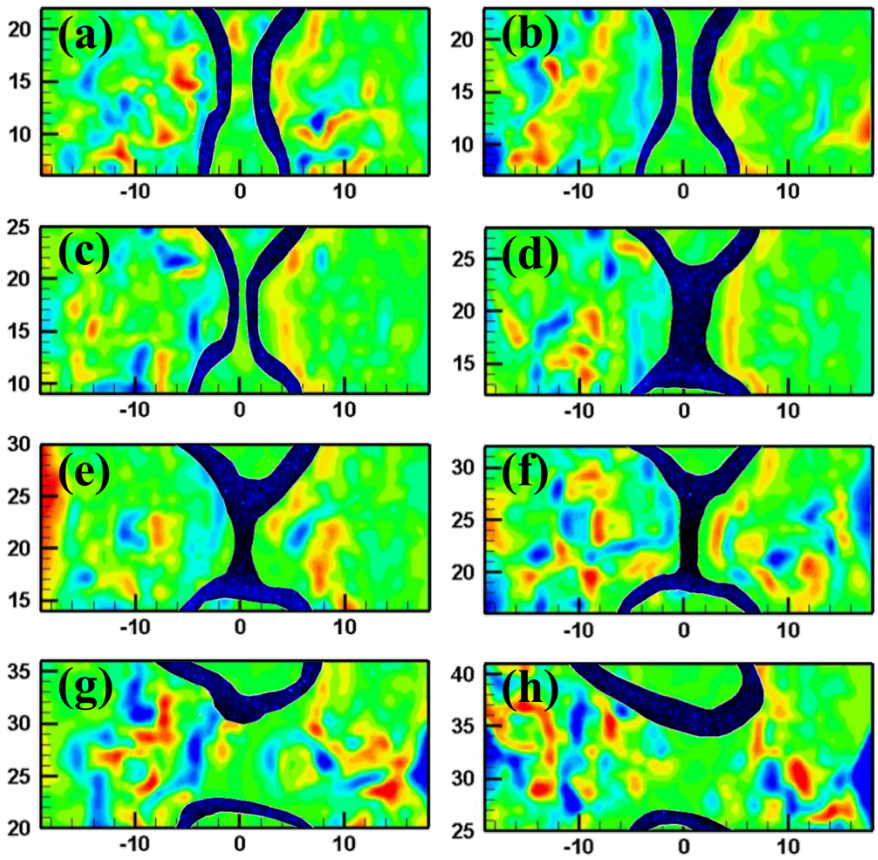

Figure 3.8 The temporal analysis with the expanded ROI.
(a) $t = 1ms$ (b) $2ms$ (c) $3ms$ (d) $4ms$
(e) $5ms$ (f) $6ms$ (g) $7ms$ (h) $8ms$.

3.2.4 Comparison of the strain rate distribution

The flame puffed process could be divided into three cases. Undeveloped case, transient case, and the fully puffed case were those. We chose the representative time for those three cases. Simultaneous measurement results were shown in Fig. 3.9. Also, each of the cases had different measurement positions which was the most critical at that time. With those measurement time and position, the strain rate distributions along the horizontal line on the measurement positions were plotted in Fig. 3.10. The representative time, the measurement positions, and the maximum absolute strain rate for the each cases were noted in the Table 3.1.

Table 3.1 Experimental condition for the strain rate distribution.

Case	**Time** $[ms]$	**Measurement position [mm]**	**Maximum absolute strain rate [1/s]**
Undeveloped case	$t = 2$	$y = 16$	876.48
Transient case	$t = 6$	$y = 24$	1355.17
Fully puffed case	$t = 7$	$y = 28$	2142.89

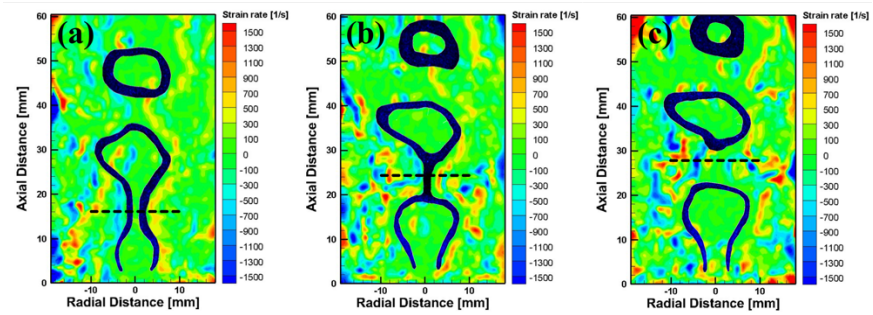

Figure 3.9 The simultaneous measurement results for the various time.

(a) $t = 2ms$ (b) $6ms$ (c) $7ms$.

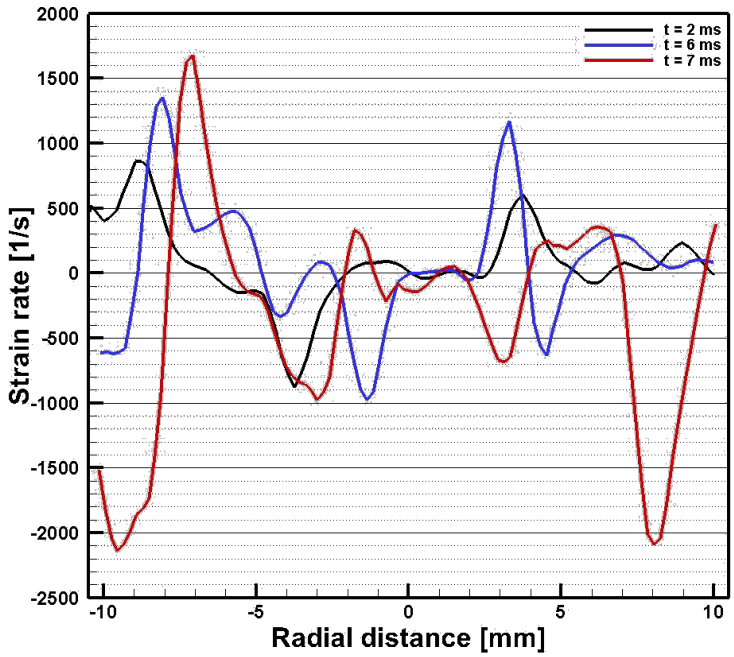

Figure 3.10 The strain rate distribution at the critical regions.

As the flame puffed process proceeded, in Fig. 3.10, the strain rate distributed at the critical regions became higher. Meanwhile, we could know the maximum absolute strain rate applied to the critical region was gradually increased.

3.2.5 The effect of the strain rate to the puffed flame throat

With the earlier results, as the flame puffed phenomenon proceeded, the relative high strain rate near the flame throat gradually invaded into the middle of the flame. The horizontal gaps between two strain rate beside the flame throat and the flame throat thickness were plotted in Fig. 3.11. At that time, the horizontal gaps between two strain rate were measured for the value over $400/s$ of strain rate. The value of $400/s$ was the average strain rate for the combustion field without any external acoustic forcing.

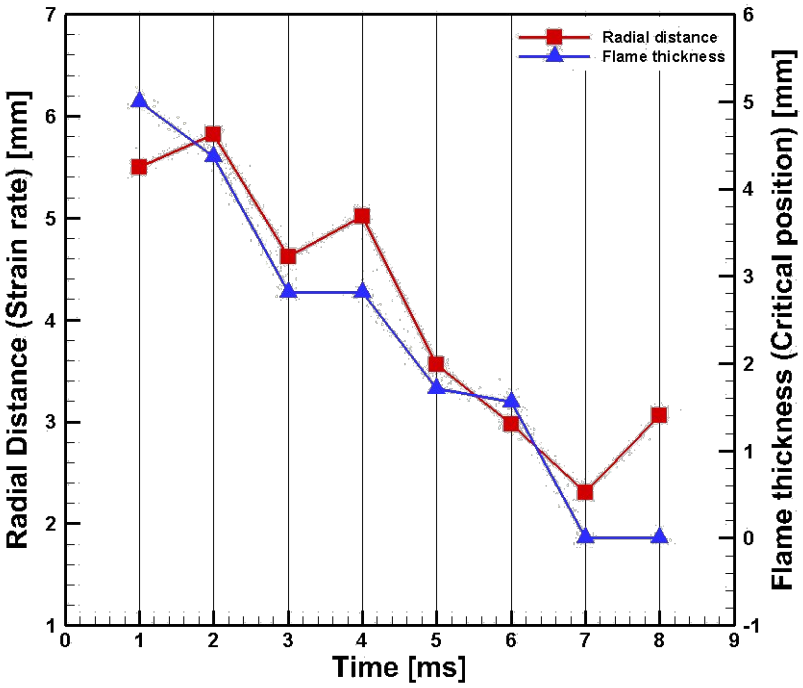

Figure 3.11 The relationship between
the flame throat thickness and the strain rate.

In Fig. 3.11, the change of the horizontal distance between two strain rate and the flame thickness had the same tendency. This meant that the flame throat thickness was decreased as the strained flow was entrained. Finally, at the time when $t = 7ms$, the flame throat thickness became zero due to the entrainment of the strained flow. Then the local extinction region was generated, as shown in Fig. 3.8 (g).

3.2.6 The maximum and the minimum strain rate

The variations of the maximum positive strain rate and the minimum negative strain rate around the critical regions were shown in Fig. 3.12. The variations of the maximum and the minimum strain rate almost had the same tendency. In addition, we could analyzed that the higher absolute strain rate was employed when the flame fully puffed. A series of this variation of the maximum absolute strain rate was repeated as a cycle, thus this tendency constantly appeared as the flame puffed phenomenon was continued. The gaps between the maximum absolute strain rates from the center line which were shown in Fig. 3.12 were plotted in Fig 3.13 as well.

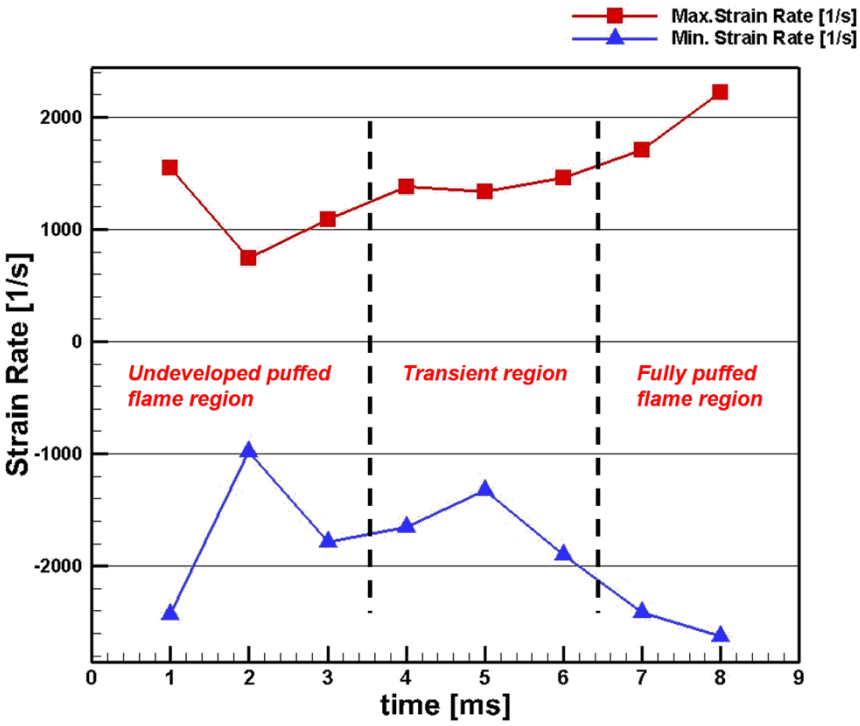

Figure 3.12 The maximum absolute strain rate during the flame puffed process.

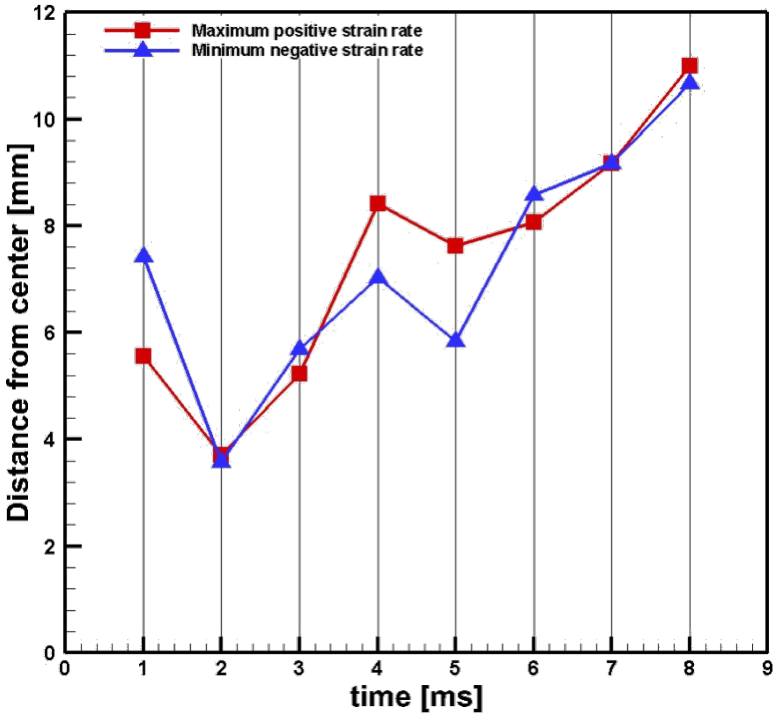

Figure 3.13 Distance from the center line of the maximum absolute strain rate.

As the flame puffed process flowed, the horizontal distance became further from the center line. In other words, the higher strain rate was located more further from the center line.

In Fig. 3.14 (a) to (c), the flame surface, the strain rate contour, and the vector field for the specific time were represented. The black hollow circles expressed where the maximum absolute strain rate was located. As shown in Fig. 3.14 (a) to (c), more irregular flow, like a vortical flow and a strong entrained flow to the local extinction region, was confirmed with the progress of the flame puffed phenomenon.

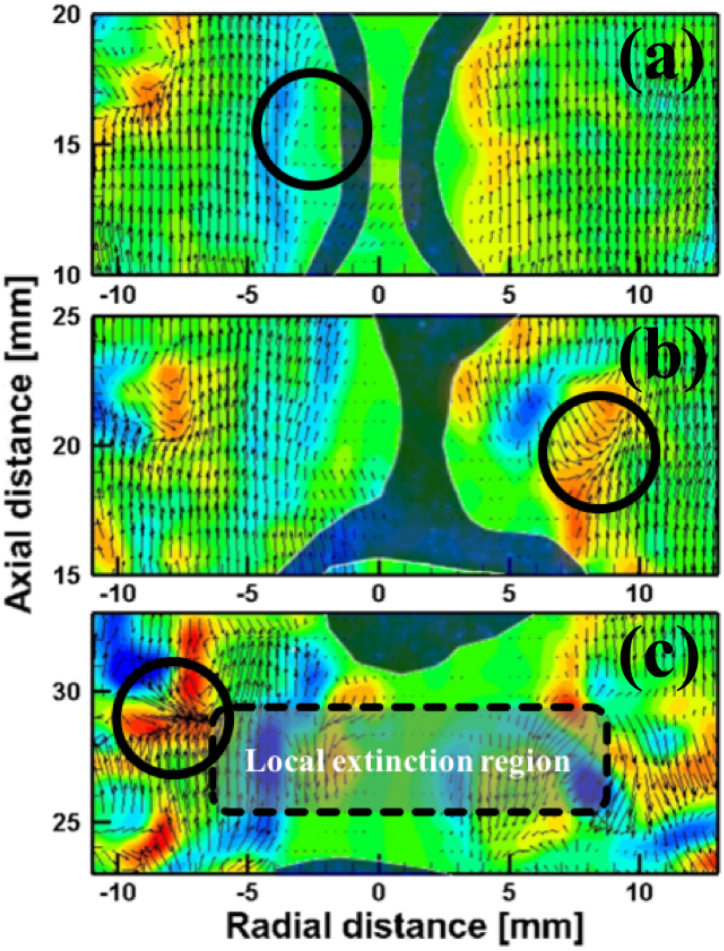

Figure 3.14 The location of the maximum absolute strain rate.
(a) $t = 2ms$ (b) $5ms$ (c) $7ms$

The generation of the turbulent-like flow was periodic characteristics of this phenomenon. Under the strong acoustic forcing, the laminar-like flow was dominant at the initial stage, then the turbulent-like flow became dominant flow characteristics with the process and then more higher strain rate was applied. This unusual flow development, the transformation from the laminar-like flow to the turbulent-like flow, was resolved with the local extinction. After that, the unusual flow development process was taken place again, as the flame puff proceeded. With this result, therefore, the surrounding air flow could be a reason for the flame puffed phenomenon.

3.2.7 Surrounding air entrainment

Surrounding air behavior played a key role as well as the strain rate did. The surrounding air entrainment process is expressed in Fig. 3.15 (a) to (d). At first, surrounding air flowed to the nearby reaction zone with the clockwise and the counterclockwise motions, as shown in Fig. 3.15 (a). The vortical flow near the flame throat dragged the air into the flame region. Simultaneously, some portion of the surrounding air pushed the flame to the downstream. In Fig. 3.15 (b), the surrounding air entrained to the middle of the reaction zone. The flame throat, which was the highly wrinkled region, was developed due to the continuous radial and axial flow entrainment. At the next step, in Fig. 3.15 (c), the surrounding air was further entrained to the reaction zone. Just before the flame puffed, high level of downstream flow could be discovered. At the time flame fully puffed, the surrounding air was totally entrained to the reaction zone and then perfectly separated the flame, as shown in Fig. 3.15 (d). Meanwhile, the relative high strain rate was distributed in the local extinction region.

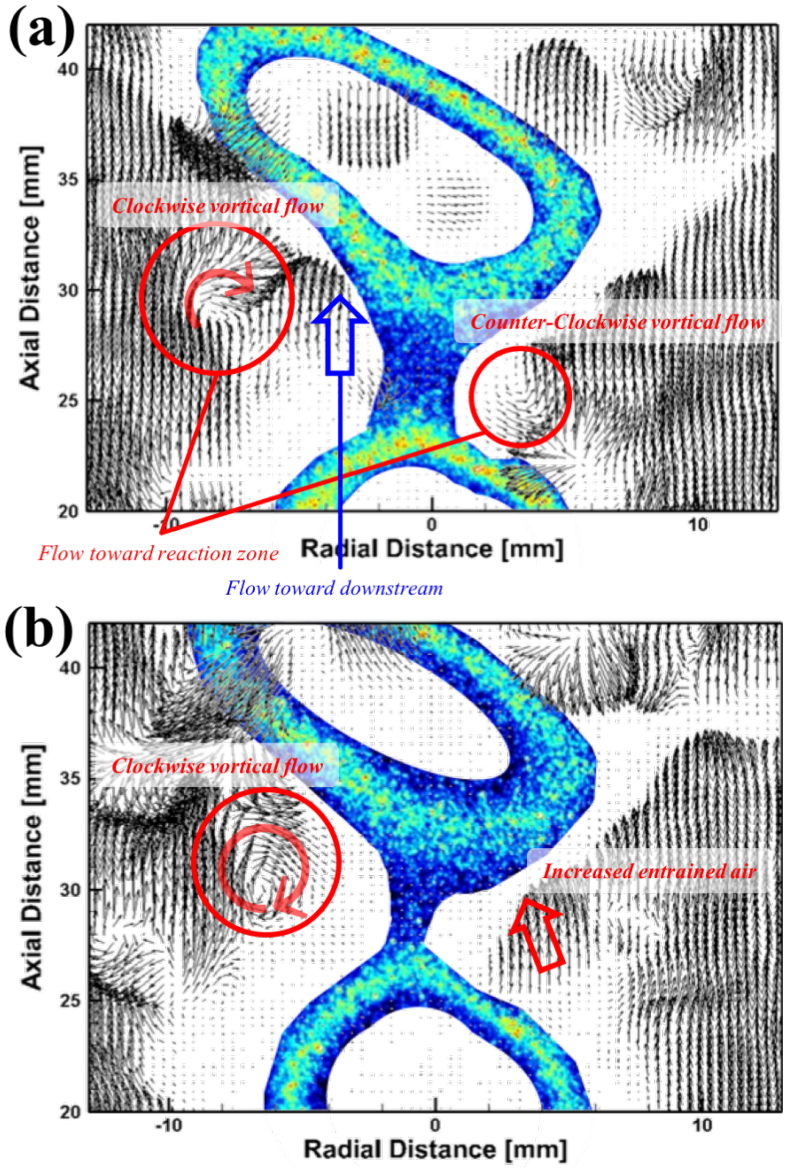
(a)
Axial Distance [mm]
Radial Distance [mm]
Clockwise vortical flow
Counter-Clockwise vortical flow
Flow toward reaction zone
Flow toward downstream
(b)
Axial Distance [mm]
Radial Distance [mm]
Clockwise vortical flow
Increased entrained air

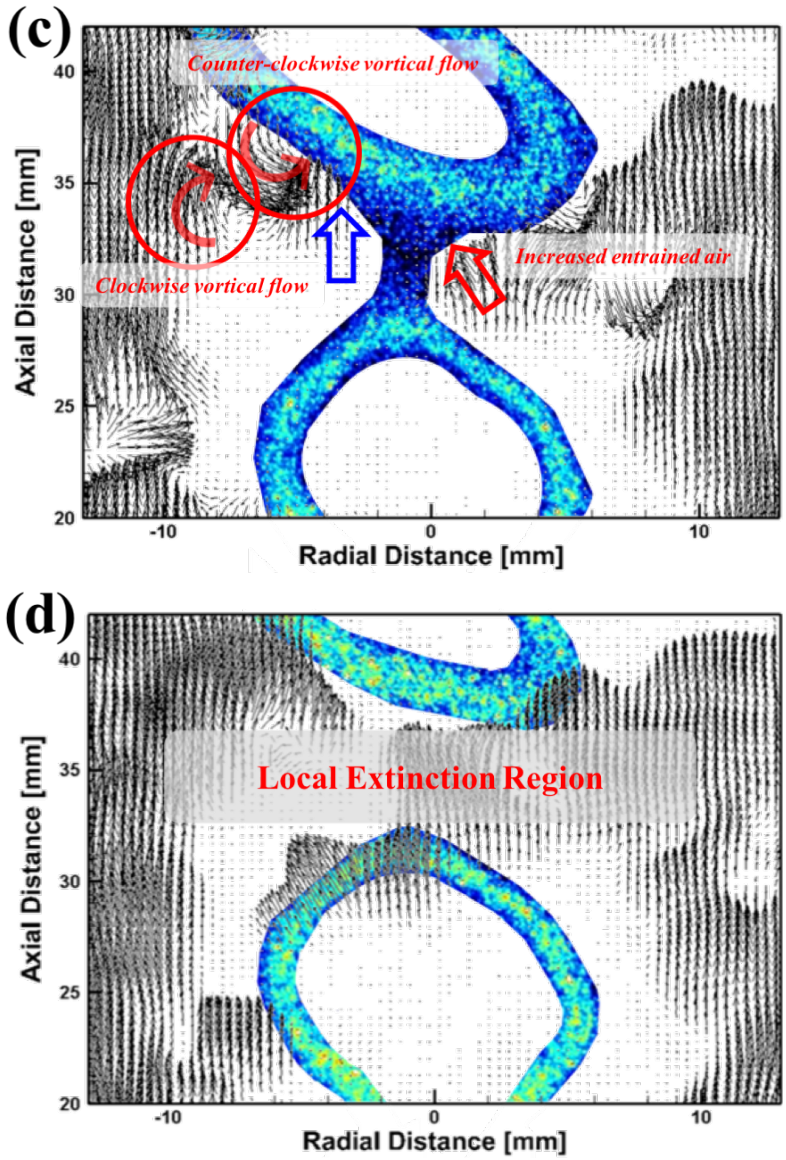

Figure 3.15 The process of the surrounding air entrainment.

(a) $t = 4ms$ (b) $5ms$ (c) $6ms$ (d) $7ms$

3.3 Dynamic characteristics of the puffed flame

To analyze the response characteristics of the puffed flame, the flame length and the flame surface area were measured from the OH-PLIF images. Also, the flame length perturbation and the surface area perturbation were calculated.

$$flame\ length\ perturbation = {l'}/{\bar{l}} \qquad (13)$$

$$flame\ surface\ area\ perturbation = {S'}/{\bar{S}} \qquad (14)$$

When the flame length and the surface area were calculated, the threshold of the images was 10 percent. The intensity of the pixel which was lower than 10 percent of the maximum was turned into zero. The images used to determine the length and surface area were the averaged images during the 100 periods.

3.3.1 Flame length and surface area

Changing the acoustic forcing frequency, in Fig.3.16 (a), the flame length for the various velocity perturbation amplitude were calculated. In the cases of each forcing frequencies, the tendency, that the flame length decreased as the velocity perturbation increased, was almost same. For the puffed flame cases, however, significant decrease of the flame length was confirmed. Similarly, the flame surface area also decreased considerably for the puffed flame cases, as shown in Fig. 3.16 (b).

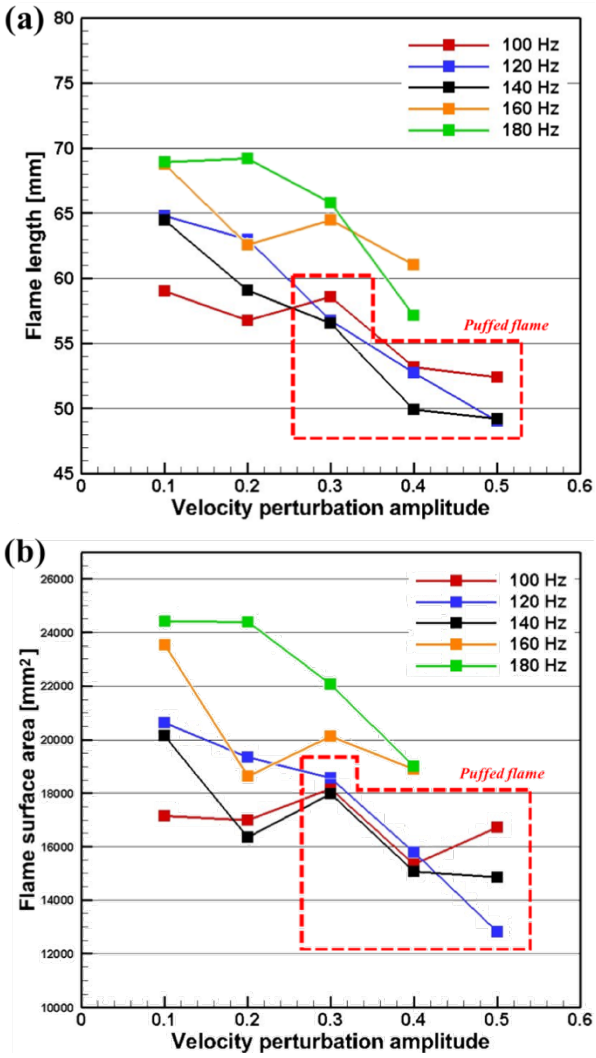

Figure 3.16 Flame response characteristics for various frequencies and the amplitudes.
(a) Flame length (b) Flame surface area

Forcing frequency dependence of the flame length and the surface area was analyzed for 0.3 and 0.4 of the velocity perturbation in Fig. 3.17 (a) and (b). The flame puffed phenomenon was occurred at the forcing frequency of 100 Hz to 140 Hz when the velocity perturbation amplitude were 0.3 and 0.4, as already known. When the flame puffed phenomenon was occurred, the flame length and the surface area decreased drastically. There was a significant contrast in the flame response characteristics between the puffed flame and the flame which was only wrinkled.

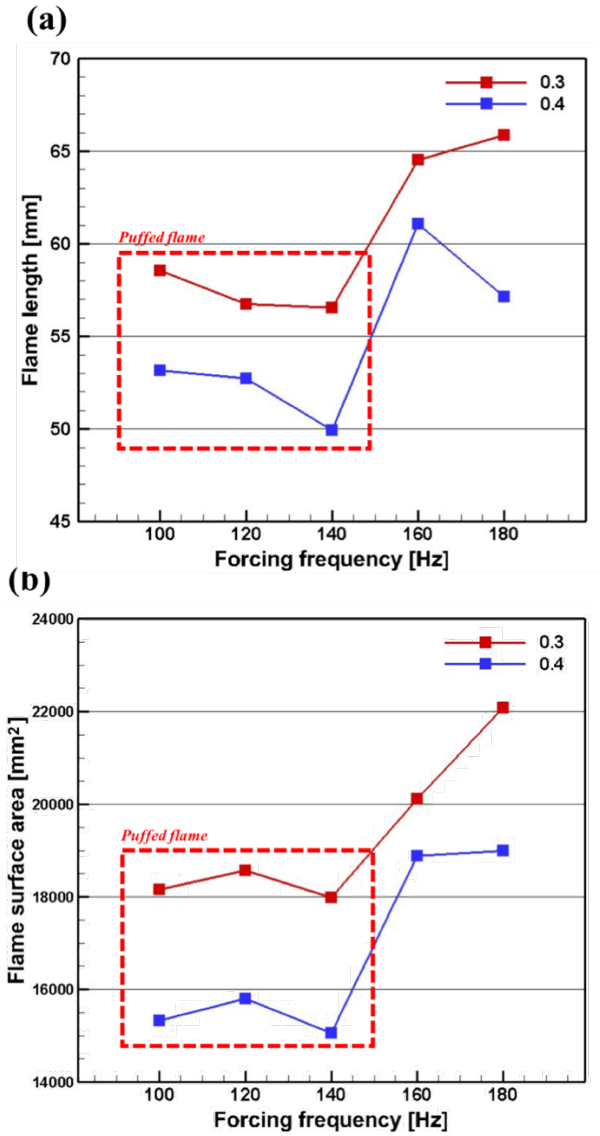

Figure 3.17 Flame response characteristics for various forcing frequencies at the velocity perturbations of 0.3 and 0.4.
(a) Flame length (b) Flame surface area

3.3.2 Flame length and surface area perturbation

The flame length perturbation and the surface area perturbation were measured in Fig. 3.18 (a) and (b). For the puffed flame cases, both of the perturbations were more bigger than the other cases. From those results for dynamic characteristics for the puffed flame, we could stand out the flame became more unstable when the flame puffed phenomenon was occurred.

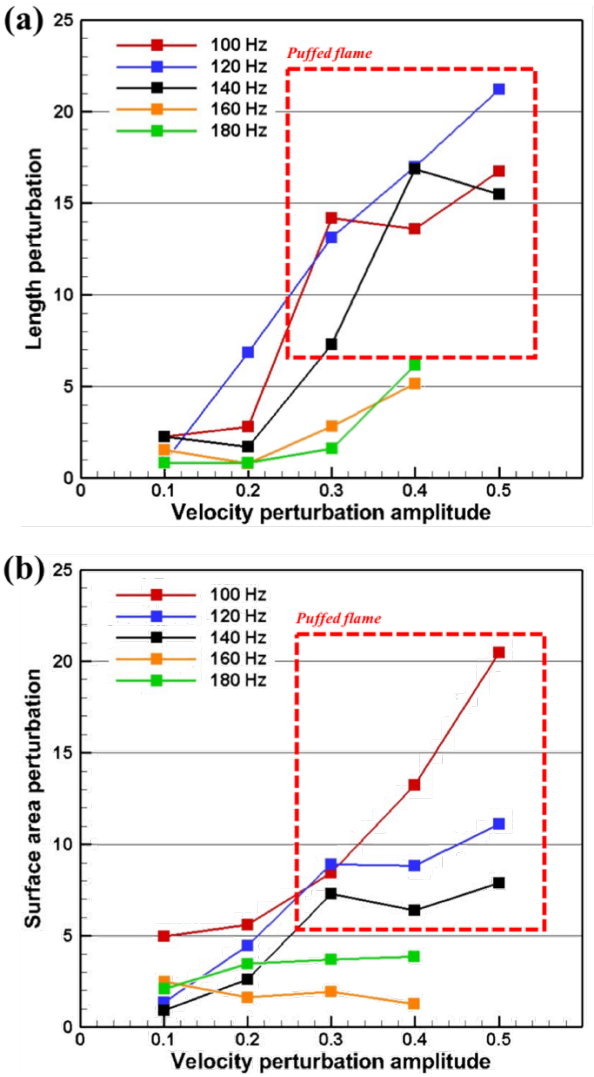

Figure 3.18 Perturbations of the flame characteristics for various amplitudes and the frequencies.
(a) Flame length perturbation (b) Flame surface area perturbation

Chapter 4. CONCLUSION

The present research investigated for the causes of the flame puffed phenomenon and its dynamic characteristics. This research was conducted for the various forcing frequencies and the velocity perturbation amplitudes. To analyze the puffed flame process and the characteristics, simultaneous PIV and OH-PLIF measurement was applied. With the laser diagnostics, simultaneous OH distribution, vector field, and strain rate field could be obtained. Because of these properties, we could analyze the effect of the strain rate and the surrounding air entrainment. Also, the response characteristics for the puffed flame was observed.

(1) From the OH-PLIF results, the puffed flame was easily occurred in the lower frequency region and the higher velocity perturbation amplitude region. The flame puffed phenomenon had a periodic characteristics following the acoustic forcing wave because this phenomenon was due to strong external acoustic excitation.

(2) From the simultaneous OH-PLIF and PIV measurement, the strain rate effect and the surrounding air entrainment played key roles for the flame puffed.

(3) As the flame puffed process proceeded, more higher strain rate was applied to the flame surface. For the critical region (flame throat), the maximum positive strain rate and the minimum negative strain rate had a same tendency. Then, this high strain rate made the flame throat thinner.

(4) During the process, surrounding air flow transformed to the turbulent-like flow from the laminar-like flow (i.e. more irregular flow was detected). Also, it was a periodic behavior. Surrounding air gradually invaded into the middle of the flame region, therefore flame was separated in two regions (major flame region and secondary flame region) finally.

(5) Flame puffed phenomenon was a periodic phenomenon and was developed with such steps.

1. With strong acoustic forcing, radial velocity components of the flow were generated.

2. Due to these radial velocity components of the flow, flame started to wrinkle.

3. Relative high strain rate was distributed along the flame surface and the distributed strain rate increased as the process proceeded.

4. Meanwhile, surrounding air with the irregular flow gradually invaded into the middle of the flame region

5. With those high strain rate and the surrounding air entrainment, flame was finally separated into the major region and the secondary region.

(6) Flame length and the surface area significantly decreased when the flame puffed phenomenon was occurred. However, flame length and surface area perturbation were increased for the puffed flame cases. Thus, puffed flame should be more unstable than the normal flame which was formed without external acoustic excitation.

Appendix A. Theoretical Understanding of Resonance Frequency

A.1 One-dimensional Wave

Consider the wave equation for velocity : [24]

$$\frac{\partial^2 v}{\partial x^2} = \frac{1}{c^2}\frac{\partial v}{\partial t^2} \tag{A.1}$$

In this case, assume that a separable solution exits such that

$$v = X(x)T(t) \tag{A.2}$$

Then substituting equation A.2 in to equation A.1 yields

$$T\frac{\partial^2 X}{\partial x^2} = \frac{x}{c^2}\frac{\partial^2 T}{\partial t^2} \tag{A.3}$$

And dividing XT

$$\frac{1}{X}\frac{\partial^2 X}{\partial x^2} = \frac{1}{c^2 T}\frac{\partial^2 T}{\partial t^2} \tag{A.4}$$

Now the right side of this equation is a function of t only, while the left side is a function of x only. However x and t are independent variables. So both sides of the equation must be equal to a constant, $-k^2$, say.

Then

$$\frac{\partial^2 X}{\partial x^2} = -k^2 X \tag{A.5}$$

And

$$\frac{\partial^2 T}{\partial t^2} = -c^2 k^2 X \tag{A.6}$$

These equations have the same form as the harmonic motion equation, and letting

$$ck = w \text{ or } c = w/k \tag{A.7}$$

We obtain the solution of equation A.6:

$$T = Ae^{jwt} + Be^{-jwt} \tag{A.8}$$

For a physically meaningful solution, B = 0. Similarly, for equation A.5

$$X = Ce^{jwt} + De^{-jwt} \tag{A.9}$$

And finally

$$v = A_1 e^{j(wt+kx)} + Be^{-j(wt-kx)} \tag{A.10}$$

This expression than is a general solution of wave equation, which is both consistent with D'Alembert solution and is separable. Here,

$$e^{j(wt+kx)} = \mathrm{Cos}(wt + kx) + \ j\sin(wt + kx) \tag{A.11}$$

A.2 Modes of a tube

The general solution of the one-dimensional wave equation for velocity is

$$\begin{aligned} v &= A_1 e^{j(wt+kx)} + Be^{-j(wt-kx)} \\ &= e^{jwt}[C\cos(kx) + D\sin(kx)] \end{aligned} \tag{A.12}$$

The boundary conditions for a tube with rigid caps are

$$v = 0, \text{when } x = 0 \tag{A.13}$$

so that

$$C = 0 \tag{A.14}$$

and than

$$v = De^{jwt}\sin\,(kx) \tag{A.15}$$

Also, another boundary condition

$$v = 0, \text{when } x = l \tag{A.16}$$

$$\text{Sin}(kl) = 0 \tag{A.17}$$

and

$$kl = n\pi, \text{or } l = n\lambda/2 \tag{A.18}$$

so the frequency at these modes of oscillation occur are

$$f = \frac{nc}{2l} \tag{A.19}$$

The boundary conditions for a tube with one open end and one close end are

$$v = 0, \text{when } x = 0 \tag{A.20}$$

so that

$$C = 0 \tag{A.21}$$

and than

$$v = De^{jwt}\sin(kx) \tag{A.22}$$

Also, another boundary condition

$$\frac{dv}{dx} = 0, \text{when } x = 1 \tag{A.23}$$

$$k\cos(kl) = 0 \tag{A.24}$$

and

$$kl = \frac{(2n-1)\pi}{2}, \text{or } l = \frac{(2n-1)\lambda}{4} \tag{A.25}$$

so the frequency at these modes of oscillation occur are

$$f = \frac{(2n-1)c}{4l} \tag{A.26}$$

Bibliography

[1] T.S. Kim, M.G. Ahn, J.J. Hwang, S.H.Kim, and Y.B. Yoon, "The Experimental Investigation on the Response of the Burke-Schumann Flame to Acoustic Excitation," *Proceedings of the Combustion Institute,* 2017, 36(1), pp. 1629-1636.

[2] J.J. Hwang, N. Bouvet, K.T. Sohn, and Y.B. Yoon, "Stability of the Attached Flame in H_2/CO Syngas Non-premixed Turbulent Jet Flame," *Journal of the Korean Society of Combustion,* 2012, 17(1), pp. 22-29.

[3] M.G. Ahn, T.S. Kim, H.D. Kim, and Y.B. Yoon, "A Study on Response Characteristics of Jet-diffusion Flame and Premixed Flame with Various Velocity Perturbations," *Journal of the Korean Society of Combustion,* 2017, 22(2), pp. 19-26.

[4] Z. Rossel, X. Bai, J. Sjoholm, and Z. Wang, "Multi-species PLIF Study of the Structures of Turbulent Premixed Methane/Air Jet Flames in the Flamelet and Thin-reaction Zones Regimes,"

Combustion and Flame, 2017, 182, pp. 324-338.

[5] M. Shimura, T. Ueda, G.M. Choi, M. Tanahashi, and T. Miyauchi, "Simultaneous Dual-plane CH PLIF, Single-plane OH PLIF and Dual-plane Stereoscopic PIV Measurements in Methane-air Turbulent Premixed Flames," *Proceedings of the Combustion Institute,* 2011, 33(1), pp. 775-782.

[6] M. Tanahashi, S. Murakami, G.M. Choi, Y. Fukuchi, and T. Miyauchi, "Simultaneous CH-OH PLIF and Stereoscopic PIV Measurements of Turbulent Premixed Flames," *Proceedings of the Combustion Institute,* 2005, 30(1), pp. 1665-1672.

[7] A. Elbaz, and W. Roberts, "Experimental Study of the Inverse Diffusion Flame Using High Repetition Rate OH/acetone PLIF and PIV," *Fuel,* 2016, 165, pp. 447-461.

[8] K. Lakshminarasimhan, N. Clemens, and O. Ezekoye, "Characteristics of Strongly-forced Turbulent Jets and Non-premixed Jet Flames," *Experiments in Fluids,* 2006, 41(4), pp. 523-542.

[9] J. Rehm, and N. Clemens, "The Relationship between

Vorticity/strain and Reaction Zone Structure in Turbulent Non-premixed Jet Flames," *Symposium (International) on Combustion,* 1998, 27(1), pp. 1113-1120.

[10] E. Salaün, P. Malbois, A. Vandel, G. Godard, F. Grisch, B. Renou, G. Cabot, and A. Boukhalfa, "Experimental Investigation of a Spray Swirled Flame in Gas Turbine Model Combustor," *International Symposium on the Application of Laser and Imaging Techniques to Fluid Mechanics,* 2016.

[11] J. Donbar, J. Driscoll, and C. Carter, "Strain Rates Measured along the Wrinkled Flame Contour within Turbulent Non-premixed Jet Flames," *Combustion and Flame,* 2001, 124(4), pp. 1239-1257.

[12] F. Creta, and M. Matalon, "Strain Rate Effects in the Nonlinear Development of Hydrodynamically Unstable Flames," *Proceedings of the Combustion Institute,* 2011, 33(1), pp. 1087-1094.

[13] B. Coriton, and J. Frank, "Experimental Study of Vorticity-Strain Rate Interaction in Turbulent Partially Premixed Jet Flames Using Tomographic Particle Image Velocimetry," *Physics of Fluids,* 2016, 28(2), pp. 025109.

[14] X. Wang, H. Hou, and V. Yang, "Effects of Flow Strain Rates in Counterflow Diffusion Flames at Subcritical and Supercritical Pressures: Oxygen/Methane Mixture," *52nd Aerospace Sciences Meeting, 2014,* pp. 0650.

[15] Y. Cho, J.H. Kim, T. Cho, I. Moon, Y. Yoon, and C. Lee, "Analysis of Turbulent Premixed Flame Structure Using Simultaneous PIV-OH PLIF," *Journal of Visualization,* 2004, 7(1), pp. 43-54.

[16] P. Kothnur, and N. Clemens, "Experimental Investigation of the Relationship between Strain and Dissipation in Gas-phase Turbulent Jets," *39th Aerospace Sciences Meeting and Exhibit,* 2001, pp.1023.

[17] N. Chakraborty, "Statistics of Vorticity Alignment with Local Strain Rates in Turbulent Premixed Flames," *European Journal of Mechanics-B/Fluids,* 2014, 46, pp. 201-220.

[18] L, Chen, J, Seaba, W. Roquemore, and L. Goss, "Buoyant Diffusion Flames," *Symposium (International) on Combustion,* 1989, 22(1), pp. 677-684.

[19] X. Jiang, and K. Luo, "Combustion-induced Buoyancy Effects of an Axisymmetric Reactive Plume," *Proceedings of the Combustion*

Institute, 2000, 28(2), 1989-1995.

[20] X. Jiang, "Numerical Studies of Vortex Shedding in Forced Oscillatory Non-premixed Flames," *IOP Conference Series: Materials Science and Engineering,* 2010, 10(1), pp. 012030.

[21] A. Yule, N. Chigier, S. Ralph, R. Boulderstone, and J, Venturag, "Combustion-transition Interaction in a Jet Flame," *AIAA,* 1981, 19(6), pp. 752-760.

[22] P. Kolhe, and A. Agrawal, "Role of Buoyancy on Instabilities and Structure of Transitional Gas Jet Diffusion Flames," *Flow, Turbulence and Combustion,* 2007, 79(4), pp. 343-360.

[23] S. Hou, D. Chung, and T. Lin, "Experimental and Numerical Investigation of Jet Flow and Flames with Acoustic Modulation," *International Journal of Heat and Mass Transfer,* 2015, 83, pp. 562-574.

[24] N. Yoshihara, A. Ito, and H. Torikai, "Flame Characteristics of Small-scale Pool Fires under Low Gravity Environments," *Proceedings of the Combustion Institute,* 2013, 34(2), pp. 2599-2606.

[25] H. Abe, A. Ito, and H. Torikai, "Effect of Gravity on Puffing

Phenomenon of Liquid Pool Fires," *Proceedings of the Combustion Institute,* 2015, 35(3), pp. 2581-2587.

[26] Y. Liao, and J. Hermanson, "OH-PLIF Imaging of the Reaction Zone in Swirled, Strongly-Pulsed Jet Diffusion Flames with a Low Reynolds Number," *Combustion Science and Technology,* 2018, 190(4), pp. 615-631.

[27] J. Carpio, M. Sánchez-Sanz, and E. Fermández-Tarrazo, "Pinch-off in Forced and Non-forced, Buoyant Laminar Jet Diffusion Flames," *Combustion and Flame,* 2012, 159(1), pp. 161-169.

[28] G. Carrier, F. Fendell, and F. Marble, "The Effect of Strain Rate on Diffusion Flames," *SIAM Journal on Applied Mathematics,* 1975, 28(2), pp. 463-500.

초 록

열 방출량과 화염면 사이에는 일련의 관계가 존재하기 때문에 연소불안정에 대한 예측을 위해서는 화염 구조에 관한 연구가 필요하다. 연소불안정은 이를 구성하는 세 가지 섭동이 양성 피드백 루프를 형성하였을 때 발생 및 증폭하기 때문에 각각의 세 가지 섭동에 대해 자세히 고려할 필요가 있다. 본 연구에서는 연소불안정에 관한 연구의 일환으로 puffed 화염이라 불리는 특이 화염 구조에 관한 연구를 수행하였다. 이전 연구에서, 김 등[1]은 특정 주파수 및 입력 속도 섭동 영역에서 puffed 화염이 발생하는 것을 확인하였다. 따라서 본 연구에서는 이러한 puffed 화염에 관한 발생 원인과 응답 특성에 관해 연구하였다. 그에 따라, OH-PLIF 와 PIV 동시 계측을 수행하였다.

실험은 확산 화염의 한 종류인, 연료 분출 속도와 산화제 분출 속도가 서로 동일한 버크 슈만 화염에 관해 진행하였다. 메탄과 수소의 혼합기가 연료로 사용되었고 산화제로는 상온 공기가 사용되었다. 연소불안정 현상을 모사하기 위한 외부 음향 가진은 100 Hz 부터 180 Hz 까지 20 Hz 간격으로 인가되었다. 또한 입력 속도 섭동 진폭은 0.1에서 0.5 까지 0.1의 간격으로 적용되었다.

레이저 동시 계측에 의해 속도장, strain rate장, OH 분포는 동시에 계측되었다. 동시 계측의 결과로 화염의 응답 특성과 유동의 거동은 같은 시간대에 대해 분석되었다. OH-PLIF 계측을 이용하여 화염 구조를 확인하였으며 이 외의 다른 정량적 계측은 PIV 계측을

이용하여 수행하였다.

동일한 외부 음향 가진 주파수 영역에서는 특정 입력 속도 이상에서 flame puffed 현상이 발생되었다. 외부 음향 가진 주파수가 증가하는 경우에는 화염을 분리하기 위해 더 큰 입력 속도 섭동이 필요하였다. 이는 화염이 저역 필터 라는 것을 다시 한 번 알 수 있게 하였다. 또한 flame puffed 현상은 외부 음향 가진 주파수에 따라 주기적으로 발현됨을 확인할 수 있었다.

PIV와 OH-PLIF의 동시 계측을 통해 높은 strain rate 와 산화제의 유입이 화염의 절단 과정에 있어 주요한 원인이 됨을 파악하였다. 실험 결과에 따라, 높은 strain rate가 작용하면 화염면이 섭동하고 화염목이 더욱 좁아지게 된다. 또한 flame puffed 과정이 진행됨에 따라, 점점 더 높은 strain rate 가 화염면에 작용하는 것을 확인하였다. Flame puffed 과정의 마지막 단계에서 일반적이지 않은 급격한 변화를 보이는 유동이 계측되었고 이로 인해 더욱 높은 strain rate 가 화염면에 작용하였다.

이와 동시에, 화염으로의 산화제의 유입은 화염 절단 현상의 또 다른 원인이라 할 수 있었다. Flame puffed 과정이 진행되면서 주위 공기가 점차 화염 중간 영역으로 침입하였으며 이로 인해 결국엔 화염이 완전히 분리되고 산화제가 해당 영역 중간으로 완벽하게 침투된다.

Flame puffed 현상이 발생하면 화염의 응답 특성은 음향 가진을 인가하지 않은 경우와 완전히 달라진다. 화염의 길이와 면적은 보다 짧아지게 되나 화염의 길이 및 면적 섭동은 큰 폭으로 증가한다. 즉, flame puffed 현상이 발생하는 경우에 화염은 보다 불안정한 상태가

된다고 할 수 있다.

주요어: 제트확산화염, 버크 슈만 화염, 연소불안정, 화염 구조, 레이저 동시 계측, OH-PLIF, PIV, 응답 특성, Strain rate, 산화제 유입, 화염 분리

학 번: 2017-29498